EXPERIMENTAL CHARACTERIZATION OF TURBULENT FLOW AROUND CYLINDER ARRAYS

THESIS

Adam D. Harder, Captain, USAF

AFIT/GAE/ENY/07-M12

DEPARTMENT OF THE AIR FORCE
AIR UNIVERSITY

AIR FORCE INSTITUTE OF TECHNOLOGY

Wright-Patterson Air Force Base, Ohio

EXPERIMENTAL CHARACTERIZATION OF TURBULENT FLOW AROUND CYLINDER ARRAYS

THESIS

Presented to the Faculty

Department of Aeronautics and Astronautics Engineering

Graduate School of Engineering and Management

Air Force Institute of Technology

Air University

Air Education and Training Command

In Partial Fulfillment of the Requirements for the

Degree of Master of Science in Aeronautical Engineering

Adam D. Harder, B.S.

Captain, USAF

March 2007

EXPERIMENTAL CHARACTERIZATION
OF TURBULENT FLOW
AROUND CYLINDER ARRAYS

Adam D. Harder, B.S.

Captain, USAF

Approved:

Dr. Mark F. Reeder (Chairman)	date
Dr. Peter J. Disimile (Member)	date
Lt. Col. Raymond C. Maple (Member)	date

AFIT/GAE/ENY/07-M12

Abstract

This research was done as part of an effort to develop alternative fire suppressant technologies for aircraft engine nacelles. A circular cylinder array was designed, built, and placed in the AFIT roll-around low speed wind tunnel to model generic clutter inside an engine nacelle. A turbulence grid was fabricated to enable measurements of the effects of turbulence level, independent of airspeed, on the flow over different model configurations. The wind tunnel test section was 12 inches wide x 12 inches high x 24 inches long. Pressure differential measurements were taken on various cylinder configurations. The configurations included one cylinder as well as one, two, and three arrays of cylinders. Half diameter spacing was used for two and three cylinder cases, as well as an additional case at a two-diameter spacing with the three array configuration. All conditions were tested with and without the turbulence grid placed at the front of the test section. Pressure differential measurements were taken at 15° increments from $0^o - 180^o$ on the circumference of on an upstream cylinder, centered vertically on the array. Hot-wire measurements were taken with and without the turbulence grid to determine airspeed and the effect of turbulence intensity generated by the grid on the wake profile. Also, vertical traverse data was taken with the hot-wire to determine airflow characteristics behind two configurations, both with and without a turbulence grid. The first had only one cylinder installed while the second was done with three arrays spaced at a half-diameter length. Pressure and velocity measurements were used to investigate the effects caused by the upstream turbulence grid.

Acknowledgements

I would like to extend my sincere gratitude to Dr. Reeder for his guidance and insight during this project. I would also like to thank Dr. Disimile and the 46^{th}TW for sponsoring this research and providing insight to the background and value of the results of this study. None of this work would have been achievable without the assistance and vast knowledge of the laboratory technicians at AFIT. Their guidance and support in setting up test facility, building the model, and operating of test equipment proved invaluable. Finally, I would like say thank you to my parents and family for their never ending support and confidence.

Adam D. Harder

Table of Contents

List of Figures

ix

List of Tables

List of Symbols

List of Abbreviations

EXPERIMENTAL CHARACTERIZATION
OF TURBULENT FLOW
AROUND CYLINDER ARRAYS

I. Introduction

1.1   Problem Statement

The adverse environment inside an aircraft engine nacelle is highly susceptible to fires. Likewise in the region, fire suppression and prevention is difficult. Large amounts of clutter in the form of wire bundles, fuel, oil, and hydraulic lines, air ducts, engine control boxes, and nacelle ribs obstruct airflow between the outer engine side wall and the nacelle casing. These obstructions create many places for fuel to accumulate, and prevent fire suppression agents from reaching fire sources. Likewise, temperatures inside and engine nacelle can reach as high as 150° C [14]. High heat, multiple scattered fuel sources and obstructions preventing a successful distribution of fire suppressants makes the engine nacelle environment difficult to maintain.

Since the 1960's halon 1301, or trifluorobromomethane (CF_3Br), has been used to extinguish aircraft engine fires [21]. Halon 1301 contains bromine, a halogen gas. Bromine suppresses the fire by depriving it of much needed hydrogen radicals. This process drastically slows the chemical reaction time and makes halon 1301 a highly effective fire suppressant. Only a 6% concentration of halon 1301 for a half second throughout the engine nacelle is required to successfully extinguish engine fires [13]. Since only a small amount of halon 1301 is required it is a formidable solution to keep aircraft fire suppression systems light in weight. Although highly effective, halon 1301 was found to be an ozone depleting agent and was banned from production effective 1 January 1994 by the *Montreal Protocol on Substances that Deplete the Ozone Layer*.

Since the 1994 production ban of halon 1301 investigations have been made on several alternatives as potential replacements. In a 1995 study by Grosshandler et

al. various types of fluorocarbons, hydrofluorocarbons, and hydrochlorofluorocarbons where compared against the fire suppression performance of halon 1301. It was found that on average these candidates required twice as much mass and volume as halon 1301 to extinguish stabilized flames [13].

To achieve better effectiveness of a replacement for halon 1301, investigation into the turbulent flow dynamics of an engine nacelle is required. This type of investigation produced little pay-off for halon 1301 due to its high effectiveness. A better understanding of the flow characteristics inside of an engine nacelle can lead to better delivery methods of fire suppressants with greater results and the use of less material.

Successful fire extinction is accomplished when the residence time of the reactants (τ_f) is much less than the characteristic time of the chemical reaction (τ_c) [13]. This occurs when the chemical reaction takes longer than the time the reactants (fuel and oxygen) are available. This relationship can be expressed using the Damköhler number, Da.

$$Da = \frac{\tau_f}{\tau_c} \qquad (1.1)$$

When the Damköhler number is large reactants are replenished faster than the chemical reaction can take place. In this case reactants are always available and the flame can be sustained. However, a small Damköhler number indicates the reactants are not replenished fast enough to sustain the combustion process [13]. The success of fire suppression in an engine nacelle is determined by the ability to decrease the Damköhler number to a critical value where a flame would become extinct [1].

Fire suppression can be accomplished one of two ways: (1) decreasing the rate in which reactants enter the combustion area, i.e. reduce the amount of oxygen entering the region by reducing local airflow, or (2) slow the chemical reaction time by increasing the characteristic reaction time, τ_c. Slowing the chemical reaction is accomplished by ensuring more of the fire suppression agent reaches the combustion zone.

The obstructions found inside an engine nacelle create unique situations for fire stabilization and suppression. Strong flows create turbulent shear flow across obstructions in many locations, altering the way flames react and the ability to transport suppressant agents. The turbulent flow creates recirculation zones behind obstructions in which slower airspeeds are seen. Slower air speeds cause these areas to have higher reactant residence times when a flame exists and the ability to retain heat. These conditions translate to higher Damköhler numbers which indicate a location for a flame to stabilize if ignited.

The ability to transport particles of suppressant agent downstream can be expressed using a Froude number, Fr.

$$Fr = \frac{U^2}{gL_{drop}} \tag{1.2}$$

Where U is the local velocity of the airflow in the region of interest, g is the gravity of the droplet, and L_{drop} is the characteristic length of the droplet, which in this case is the diameter of the droplet. A larger Fr means a liquid droplet has more of a tendency to remain suspended in the air, while a smaller Fr indicates the droplet has a greater tendency to fall from the air.

To increase the amount of fire suppressant that travels around nacelle obstacles and reaches a combustion zone, a large Fr must be obtained. The two key components of Fr are the droplet diameter and the local air velocity. Since the local air velocity is squared, this indicates that it has a larger affect on droplet suspension. Larger droplets at slow speed fall out of flowing air while small droplets at higher speeds will remain suspended. This factor becomes important when considering faster moving air across an obstruction and a recirculation zone behind an obstruction with slow moving air.

It is evident that flow characterization of an engine nacelle will lead to improvement in the implementation of fire suppression agents. Such an analysis will provide insight to the potential reactant residence time in a recirculation zone and therefore

offer an idea of how much suppression agent would be needed. Likewise, flow characterization will give a better understanding of how much suppressant will travel past obstructions found within the engine nacelle.

1.2 Objective

The overall objective of this research is to characterize the effects of a cylindrical clutter array on upstream turbulent flow to better understand an engine nacelle environment. This information will provide insight to the ability to deliver agent and suppress fires in and around engine nacelle obstructions. The research documented here will provide comparisons to data collected in a high turbulence tunnel located at the 46^{th}TW at Wright-Patterson AFB, WPAFB.

1.3 Overview

Engine nacelle clutter was modeled using a series of staggered cylinders to represent generic engine nacelle clutter. One inch diameter cylinders were arranged perpendicular to incoming air flow in a configuration containing three vertical cylinder arrays. The cylinder arrays contained five cylinders in the upstream most array followed by six and then five again moving downstream. This configuration is a one half scale equivalent of a model used by Disimile, Tucker, Croswell, and Davis, in their work done in testing water transport past generic clutter elements [11]. The cylinder arrays were placed in an open circuit wind tunnel with a 12in x 12in test section. The model was built to allow for spacing between cylinder arrays to range from one half of a cylinder diameter up to two times the cylinder diameter. Velocity profiles within the test section were taken using a hot wire system. Likewise, pressure transducer measurements were taken at circumferential increments at various cylinder locations. The results and images are reported in this paper.

4

1.4   Preview

Previous work in this field is presented in Chapter II. Included is background in the science and engineering involved in the analysis of nacelle fire suppression. Experimentation methods and test facility setup is included in Chapter III. The results and analysis of the findings are provided in Chapter IV. Chapter V brings the entire project together and highlights major findings. Also, suggestions and insight to future work are included. The appendix contains velocity reference material.

II.   Literature Review

2.1   Background

2.1.1   Turbulent Flow Around Circular Cylinders.   The circular cylinder is one of the fundamental geometries explored in fluid mechanics. It can be linked as the basic foundation to any rounded or blunt geometry. Likewise, it is a very common geometry found in engine nacelles. Fuel, hydraulic, and oil lines as well as air ducting all have circular cylindrical shapes. However, this basic shape produces some of the most complex flow field characteristics found in the studies of fluid mechanics.

As laminar flow passes a circular cylinder very distinctive characteristics develop based on Reynolds number, Re. Reynolds number is a non-dimensional flow characterization that is the ratio of inertia forces to viscous forces [6]. It is represented by

$$Re = \frac{\rho U_\infty D_{cyl}}{\mu} \tag{2.1}$$

where ρ is the air density, U_∞ is the free-stream velocity, D_{cyl} is the cylinder diameter and μ is the air viscosity. At low Reynolds numbers, the viscous effects of the cylinder can affect the streamlines far into the flow field. Yet, the streamlines remain symmetric about the centerline of the cylinder and no separation point forms on the downwind side of the cylinder. As Re increases the region in which the viscosity effects the flow becomes smaller, and only streamlines in close proximity experience an effect. Also, as Re increases, the separation point on the cylinder begins to move forward. As the Reynolds number increases and the separation point moves forward, a recirculation zone begins to develop behind the cylinder. This recirculation zone continues to grow with Reynolds number, eventually separates and becomes an oscillating turbulent wake [18]. These effects can be seen in Figure 2.1.

A single cylinder can produce effects on a flow field even at very low Reynolds numbers. Separation points begin to move, recirculation regions begin to form, and flow mixing due to an increased shear layer can occur. All of these phenomenon can
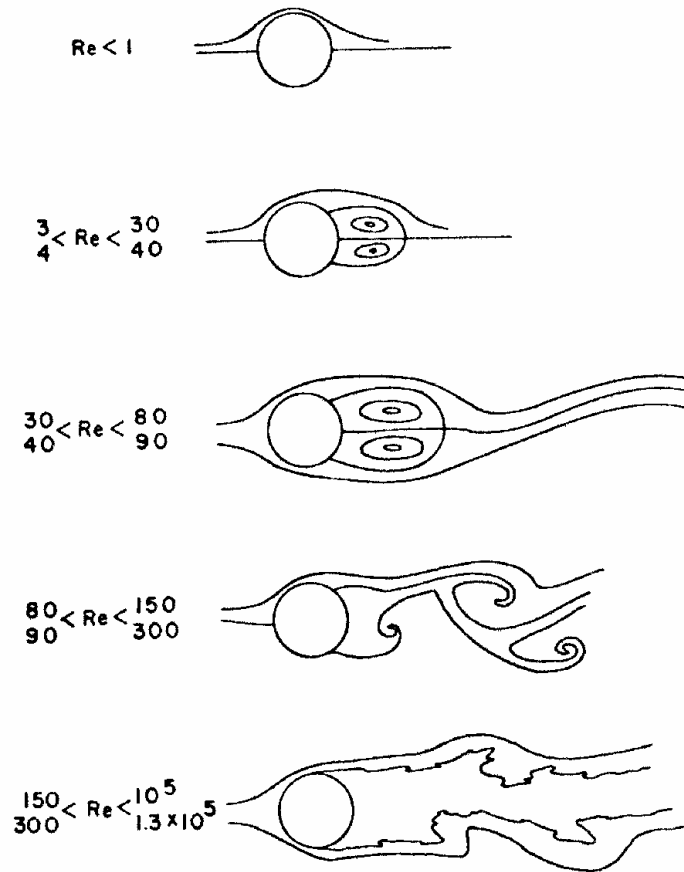
Figure 2.1:   This figure shows increasing Reynolds number effects on a circular cylinder [9].
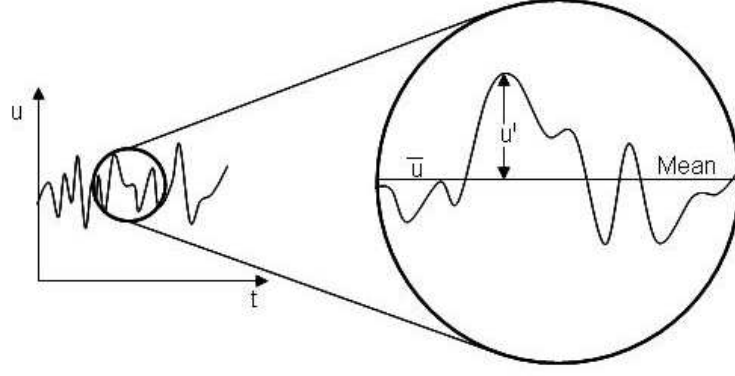
Figure 2.2:   A representation of mean flow and perturbations of airflow velocity.

effect the way flames are transported and sustained inside an engine nacelle. When the effects of one cylinder are coupled with surrounding cylinders more patterns begin to form.

Turbulent flow is characterized by a value known as turbulence intensity, TI. Turbulence intensity is a non-dimensional parameter used to quantify fluctuation intensities of the mean air flow. As air flow moves past a specific point, the magnitude of its velocity fluctuates over time. Averaged over time, a mean flow velocity develops. The difference between the magnitude of the flow velocity at a given time step and the mean velocity of the flow over the entire sample is known as the flow perturbation. The instantaneous velocity can be written as the mean flow plus the perturbation as seen in Equation 2.2

$$U_i = \bar{U} + u' \tag{2.2}$$

where U_i is the instantaneous velocity, $\bar{U}$ is the mean velocity, and u' is the perturbation. A representation of these components can be seen in Figure 2.2.

In order to calculate the TI of a flow field, a statistical analysis must be done on the mean flow and perturbation values. In Equation 2.2, U_i, $\bar{U}$, and u' represent the vector magnitude of their respective flow parameters at a specific location. These

vectors have components in all three directions. For example $\bar{U}$ can be shown as Equation 2.3 and u' can be shown as Equation 2.4.

$$\bar{U} = \bar{U}_x + \bar{U}_y + \bar{U}_z \tag{2.3}$$

$$u' = u'_x + u'_y + u'_z \tag{2.4}$$

The magnitude of $\bar{U}$ can be determined by taking the square root of the sum of the squares as seen in Equation 2.5.

$$\bar{U} = \sqrt{\bar{U}_x^2 + \bar{U}_y^2 + \bar{U}_z^2} \tag{2.5}$$

Since the perturbations have positive and negative values, a simple average of these values would result in a very small quantity. A more statistical approach is to find the root mean square, RMS, value of the components of the perturbations. This is done by taking an average of the squared values of each of the components, then taking the square root of that value as seen in Equation 2.6.

$$u'_{RMS} = \sqrt{\frac{1}{n}\sum_{i=1}^{n} x_i^2} \tag{2.6}$$

In the case of the RMS value for a perturbation with three components, Equation 2.6 becomes

$$u'_{RMS} = \sqrt{\frac{1}{3}\left({u'_{RMSx}}^2 + {u'_{RMSy}}^2 + {u'_{RMSz}}^2\right)} \tag{2.7}$$

The magnitude of $\bar{U}$ and u'_{RMS} can now be used to calculate the TI of the flow field. Turbulence intensity is defined by Equation 2.8.

$$TI = \frac{u'_{RMS}}{\bar{U}} \tag{2.8}$$

9

Table 2.1:   Iwaki Results.

	Inline	Staggered
Flow Regions	Vortex regions behind tubes Straight, high velocity streamwise between tubes	Vortex region Branching region Meeting region
Vortex patterns	Symmetric pair Asymmetric pair Large single	Symmetric pair only
Wake due to BL separation	Opened	Closed behind tubes
Turbulence Intensity(TI)	Less TI	More TI More homogeneous and isotropic More flow mixing Fully developed in short dist.

In a study by Iwaki et al. particle image velocimetry, PIV, was used to characterize the flow around tube bundles of incoming laminar flow. The study was conducted on two arrangements of tubes, inline and staggered. The results showed that very distinct patterns occurred between the inline and staggered bundles. The results were categorized into four areas: (1) flow regions, (2) vortex patterns in the mean velocity, (3) wake generation due to laminar boundary layer separation, and (4) turbulence intensities behind the second row of tubes [15]. The effects from the inline and staggered tubes can be seen in Table 2.1 [15].

The results from Iwaki et al. showed many aspects that must be kept in mind when investing flow effects and suppression requirements inside engine nacelles. A similarity between the two alignments was vortex regions forming behind all tubes. The vortex regions are created by a separated shear layer and are places of recirculation. On the other hand many difference were observed between the two alignments. First, straight, un-impinged flow was present in the inline tubes, while the flow streams in the staggered tubes met and branched from each other around each of the tubes. Second, wakes behind the inline tubes were open, creating a recirculation region trapped between two tubes. However, behind the staggered tubes, the wakes were closed, confining the recirculation region to only one tube. Finally, even though a high turbulence

intensity was present behind the inline tubes, the TI was much greater behind the staggered tubes. Likewise, the turbulent flow was more homogeneous, more isotropic, and more mixing took place in the staggered array [15]. Homogeneous turbulence implies that the "mean properties...do not vary with position" [5] and a small amount of new turbulence is being created in this region. Isotropic turbulence implies that the turbulence does not exhibit a trend to traveling in any specific direction [5]. In other words, homogeneous isotropic turbulence does not have a bulk flow in any certain direction and mean velocities are mostly due to dissipation.

2.1.2   Flame Stabilization and Extinction.   In order to extinguish a flame inside an engine nacelle it is important to understand first, what causes the flame to become stabilized and second, what conditions are necessary to extinguish the flame. Likewise, it also important to know other phenomenon that could occur in unique situations found inside an engine nacelle.

A stabilized flame occurs when the flow of the fuel and oxygen air mixture moves at a rate that is equal to the propagation velocity of the reaction [12]. Propagation velocity can also be called the laminar flame speed, S_L. Laminar flame speed is the "velocity at which unburned gases move through the combustion wave" [12]. When unburned fuel mixtures move through the reaction zone faster, more fuel becomes available to the chemical reaction. This increase in fuel results in high temperatures in the reaction zone. As temperatures increase, more radicals are produced and the characteristic time of the chemical reaction, τ_c, is shortened. Therefore τ_c is inversely proportional to the laminar flame speed as seen in Equation 2.9.

$$\tau_c \propto \frac{1}{S_L} \tag{2.9}$$

The above correlation is helpful in analyzing a laminar diffusion flame. Since turbulent flow is abundant inside engine nacelles an understanding of the turbulent flame speed, S_T, is required.

11

Many things happen in turbulent flow that can effect the chemical reaction of a flame. The extensive mixing that occurs in turbulent flow leads to perturbations in not only the flow velocity components as discussed above, but also temperature, pressure, density, and in the concentration when a fuel-air mixture is present [12]. Luckily historical analyses have shown certain trends between S_L and S_T. Knowing these comparisons allow for an easier analysis of S_T.

A correlation exists between S_L and S_T such that S_T will always be greater than S_L. German chemist Gerhard Damköhler proposed that S_T was larger than S_L through the relation expressed in Equation 2.10 [12].

$$S_T = S_L + u'$$ (2.10)

This linear correlation between S_L and S_T holds true for small turbulence intensities at a fixed Re. However, as turbulence intensity increases the relationship between S_L and S_T tapers off. Once a certain level of turbulence intensity is reached, additional increases in S_T are not seen [12]. Glassman notes that this trend was reported by P.D. Ronney in "Lecture Notes in Physics" and an example of this can be seen in Figure 2.3, which was taken from Glassman [12]. Furthermore, at higher levels of turbulence intensity, not only does S_T increase at a diminished rate, but extinction may happen when turbulence intensity reach high enough levels.

Another means for a flame to become stabilized is to become entrapped in a recirculation zone. In recirculation zones high heat levels of the combustion products ignite incoming fuel-air mixtures [12]. For this reason recirculation zones are the most predominant areas where flame ignition can occur and likewise, the most difficult to control. An occurrence known as bluff-body stabilization occurs behind obstacles such as fences, cylinders, and vee gutters. A sketch of a recirculation zone behind a single cylinder can be seen in Figure 2.4 (a), taken from Glassman [12].

Multiple cylinders in an area where a flame has been ignited and stabilized leads to additional effects on the combustion zone. Figure 2.4 (b), taken from Glassman [12],

12
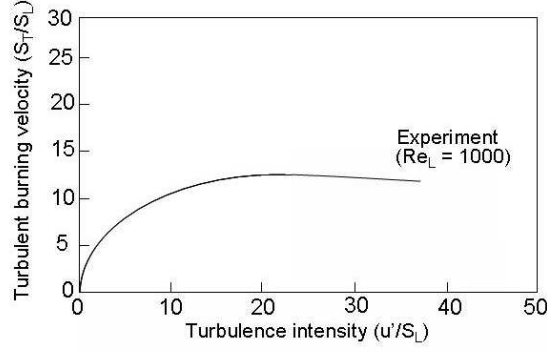
Figure 2.3:   An example of the general relationship between turbulent burning velocity and turbulence intensity, taken from Glassman [12].

(a)   (b)
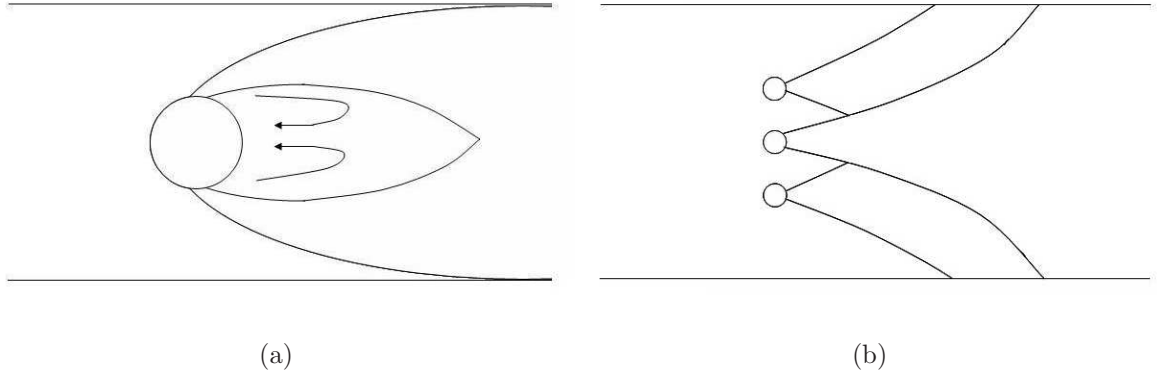
Figure 2.4:   (a) A sketch of a recirculation zone behind a single cylinder, and (b) Flame spread interactions, both taken from Glassman [12].

shows how a flames could spread downstream from multiple cylinders and interact with each other. Not only is there a potential for a flame to translate to a neighboring cylinder, but also spread downstream and interact with other engine components.

    2.1.3   Liquid Droplet Suspension in Air.   An important part of distributing fire suppressant to the location of a fire inside an engine nacelle is the ability to keep the suppressant suspended in the air long enough to reach the desired area. The ability of a liquid droplet to remain suspended in an airflow depends on the size of the droplet and the velocity of that airflow. This phenomenon can be characterized using the Froude number shown in Equation 1.2. The Froude number is a ratio between a

13

particles inertial forces and gravitational forces. Larger, slower particles with small Froude numbers will fall from the air in which they are suspended. While, smaller and faster particles will remain suspended in the air.

Unfortunately for the delivery of a fire suppressant in an engine nacelle, the answer is not as simple as minimizing or maximizing the Froude number. There are several factors taking place not only inside the engine nacelle but also with the particle droplets suspended in the flow. In order to get the suppressant past an obstruction, Fr should be large, the particle should be smaller, and the flow should be faster. However, in regions just past obstructions where circulation regions exist, there is is greater potential for a stabilized flame to exist. In this case, where the local flow is slower, a larger particle with smaller Fr would be desired to get the suppressant to fall from the air. A delicate balance of Fr is required to ensure passage of the suppressant past an obstruction, but not past the location of the flame.

There are three factors that can affect a particle size while suspended in flow. These are nucleation, coalescence, and particle size growth on the surface of an obstruction being impinged by the flow [3]. All of these phenomenon can have an effect on fire suppressants altering their ability to extinguish a flame.

Nucleation is the phase change of a substance at a localized point. In the case of an engine nacelle, nucleation of the suppressant could take place if evaporated particles met an air condition colder or slower than the one they were previously in. This could be caused by turbulent shear flow or pressure changes caused by obstructions. During nucleation, higher temperature regions can cause the suppressant to evaporate reducing the amount of effective suppressant in the flow. On the other hand, colder temperatures cause condensation and an increase of effective suppressant, much like rain drops in the atmosphere.

Coalescence occurs when suppressant droplets collide with each other in the flow. Depending on the characteristics of the suppressant droplet, substantial droplet collisions could coalesce into larger droplets increasing their potential to fall from the

flow. Likewise, as multiple droplets impinge on obstructions inside the engine nacelle, they will collect and coalesce. As these particles collect, the droplets increase in size on the surface of the obstruction, until they are to large to be re-entrained in the airflow and fall to the bottom of the nacelle.

Interestingly enough , there is a market for devices that eliminate sustained particles in airflow. These devices are used in removing particles in applications such as hydraulic sprayers, surface evaporation, saturated vapors, and chemical reactions. Separators are designed with mesh and vane style units, that act as filters for the incoming airflow [3]. Research involved in developing these types of devices applies to the application of trying to keep fire suppressant particles entrained in airflow. The application simply desires an opposite outcome.

2.2 Historical Perspective

2.2.1 Next Generation Fire Suppression Program. Since the 1994 production ban on halon 1301, research has been conducted in a wide variety of fields pertaining to engine nacelle fire suppression. At the forefront of this investigation is the Next Generation Fire Suppression Technology Program (NGP). The NGP is a Department of Defense (DoD) program initiated in 1997 to investigate and develop suppressant replacements and application techniques that are cost effective, environmentally sound, and safe for users and operators [2]. Areas of investigation have included flame suppression, physical and chemical properties of various candidate suppressants, injection techniques, and flow dynamics inside the engine nacelle.

In 2004, 25 experiments were conducted at the Ground Engine Nacelle Simulator at WPAFB. The tests involved a scale mock-up of a NAVAIR F-18 E/F engine nacelle. Various cylinders, boxes, and rib spars were in place to represent typical objects found in an engine nacelle. Pools of JP-8, situated downstream of the ribs, were set on fire while extinction time for each test case was monitored. HFC-125 was used for each test, while "mass of suppressant in the storage bottles, discharge rate of the agent, air flow, and one-at-a time capping of...agent injection nozzles" [2] were changed to get a

better understanding of suppression effects. Tests were concluded and a comparison was done to a previous computational model which used the Vulcan CFD model. While final results were not prepared by the publication of the NGP FY05 report, initial results showed some regions in the nacelle had much lower mole fractions of suppressant, indicating a significant impact from clutter and obstructions [2].

The NGP came to a close in 2006 and will present its findings in a final report available in 2007. The NGP report will be the foundation for incorporating new approaches and materials to the problem of engine nacelle fire suppression. Unfortunately one solution will not solve all of the questions to effective fire suppression. Being able to predict and model nacelle fires will lead to faster and more efficient suppressant to individual applications. Understanding the effects of turbulent flow through generic clutter will add to NGP's foundation and help provide a link to modeling such an environment.

2.2.2 Halon Alternatives. Several attributes made halon 1301 such a popular solution for fire suppression over the last few decades.

> It can be stored...as a liquid at room temperature and pressures greater than 1.61 MPa; it is a gas at atmospheric conditions, allowing to be dispersed quickly leaving no residue; it has low toxicity in pure form; it can be produced at a reasonable price in high quantity [13].

Halon 1301's greatest attribute however is how highly effective it is at extinguishing fires. Due to it's ability to extinguish fires, very little is required. This translates into smaller, lighter, and therefore cheaper storage and distribution systems for the suppressant.

The effectiveness of halon 1301 lies in the bromine contained within it's chemical composition. Bromine is a halogen gas which has one missing electron in its outer shell. Due to this missing electron, halogens easily bond with free electrons. The rate of a combustion process is determined by the amount of free hydrogen radials available to the combustion. When there are more hydrogen radicals available, the combustion reaction time will increase. Bromine combines with free hydrogen radicals taking

them away from the combustion process. With enough halogens present, hydrogen radicals can be robbed to the point of extinguishing the flame.

In an experiment conducted by Grosshandler et al., 11 different agents were tested and compared to halon 1301. The mass fraction and volume required to extinguish similar flames was compared. Due to the chemical properties of halogens expressed above, the fluorine based alternatives were tested. Four fluorocarbons (FC) were tested, five Hydro-Fluorocarbons (HFC), and and two Hydro-Chlorofluorocarbons (HCFC) were tested. Chlorofluorocarbons (CFC) are a well known ozone depleting substance. However, HCFC's have hydrogen atoms still attached, only have 10% the effect on the ozone as CFC's. Further, when no chlorine is present HFC's are formed. HFC's are not known to have any affect on the ozone [17].

Out of the 11 agents tested the hydro-chlorofluorocarbons were determined to require the least mass and volume to extinguish the flame. However, overall it was found that approximately twice the amount of mass and volume of the fluorine based agents was need to extinguish the flame [13]. This is most likely due to the fact that the bond between fluorine and hydrogen is very strong. This bond leads to a terminating reaction in the combustion process and inhibits the propagation of the chain reaction of the hydrogen radicals. Without continued propagation of hydrogen radicals the flame cannot be sustained.

2.2.3 Engine Nacelle Fire Suppression. Investigation of alternative fire suppressants to replace halon 1301 have shown that replacements exist that are effective and are not harmful to the environment. However, even the best substitutes require almost twice as much mass and volume as halon 1301. In order to keep suppressant systems light, and cost down, saturating the area is no longer an option. More effective delivery techniques are required.

Various studies have been done to investigate suppressant dispersion through a simulated engine nacelle. In an effort initiated by the 46th Test Wing at WPAFB [10] and continued by Brantley [7], an engine nacelle fire downstream of a rib spar was

17

modeled using a narrow 2-D wind tunnel with a fence protruding into the flow stream. A pool of ethanol was lit downstream of the fence while turbulent air was generated using a grid upstream of the test section.

In the 2-D tunnel, the 46^{th}TW and Brantley were able to show that a recirculation zone does exist in the area where the fuel was located, just downstream of the fence obstruction. Also, it was shown that the recirculation zone extended the entire length of the fuel pan used to hold the fuel pool. An interesting discovery showed that flow originating downstream of the obstruction was able to move back upstream, travel past the fence, and become entrapped in a recirculation zone on the upstream side of the fence. They were able to show multiple recirculation zones in which a flame could become sustained, highlighting the difficulty of predicting engine nacelle flame transport.

Takahashi et al. conducted an investigation similar to the ones done by the 46^{th}TW and Brantley. However, instead of testing flow effects past a fence obstruction, Takhashi et al. investigated the effects of the flame regions with a backward facing step obstruction. The step was a step down in the direction of the flow. Takahashi was able to again show a stabilized flame and two distinct zones of behavior when extinguished with halon 1301. In zone I, attached to the top rim of the step, the flame is extinguished by blow-out in the shear layer. However in zone II, a region where a flame is stabilized in the wake created by the down-step, the flames extinguish consecutively through the shear layer and the recirculation zone. It was determined that the mass of the agent required to extinguish the flame is equal to the characteristic mixing time of the combustion region. It was also determined that as the recirculation zone grows, more suppressant mass is required to extinguish the flame [20].

In another study by Crawford et al., CFD was used to model fire suppression experiments previously tested by spraying nitrogen in an idealized engine nacelle to extinguish a flame. In the study the space between two interlaid cylinders were used to represent the thin area found in an engine nacelle. A Tee injection nozzle as well as

a round injection nozzle were used to show how different types of suppressant delivery devices could affect the flow. Also, they were able to add a circular ring down stream to the suppressant injection point to simulate a rib spar. It was found that the CFD model was able to accurately represent experimental data. Turbulent air was used in the experiment and in the CFD simulation, however further investigation could be done with multiple clutter elements [8].

2.3 Hot-wire CTA

Hot-wire Constant Temperature Anemometry (CTA) can be used to gather mean velocity data in fluid flow. The entire hot-wire CTA system consists of the hot-wire probe, the CTA data acquisition module, the analog-to-digital converter, and the computer control system. Combined, this system is capable of measuring and processing velocity data through voltage changes generated temperature changes as flow passes over the hot-wire probe.

The hot-wire probe is placed into the flow and is held at a constant temperature through an applied voltage by the CTA system. As the flow passes over the hot-wire, its temperature will change based on the velocity of the flow. The CTA adjust the voltage to maintain the temperature of the probe wire. This voltage is then recorded and sent to the CTA module. Based on the calibration of the system, this voltage can then be used to calculate the velocity of the flow. Using probes with multiple hot-wires allows for velocity analysis in multiple components of the flow.

The correlation between voltage output and velocity can be expressed as a polynomial expression.

$$U = C_0 + C_1 E + C_2 E^2 + C_3 E^3 + C_4 E^4 \qquad (2.11)$$

Where U is the velocity, E is the output voltage, and the C's are coefficients established by the manufacturer of the system [16]. This correlation is established when

the hot-wire is calibrated and is then used to calculate velocities based on voltage output.

Unfortunately the hot-wire probes are very sensitive and can be influenced by things such as dirt contamination in the flow, vibrations, even temperature variations within the test area. Likewise, the probe is sensitive to directional alignment. The hot-wires rely on the principles of convective heat transfer to operate. Convective heat transfer is a function of surface area. If the surface area of the hot-wire is changed, i.e. if the wire is turned or tilted, the voltage output could be different. When using a multiple hot-wire probe, effective velocity can be a function of the components of flow calculated by each of the wires. The effective flow can be expressed as

$$U_{eff} = U_x^2 + k^2 U_y^2 + h^2 U_z^2 \qquad (2.12)$$

Where U_{eff} is the effective velocity U_x, U_y, and U_z, are the component velocities and k and h are yaw and pitch coefficients established during calibration [16]. Equation 2.12 is determined for each of the wires.

The CTA module maintains the hot-wire's constant temperature and voltage variations. The analog voltage response is converted to a digital signal through the A/D converter. The digital signal then sent to the compute for processing. Here the voltage and directional conversions are stored. Data reduction is done on the raw data and displayed as component velocities.

III. Experimental Setup

3.1 Wind Tunnel

The wind tunnel used in this investigation was an Aerolab Educational Wind Tunnel (EWT). A schematic of the wind tunnel is shown in Figure 3.1. The Aerolab is a 15ft long open circuit wind tunnel with a rectangular test section. The test section is 12in wide, 12in high, and 24in long. The tunnel has a 9.5:1 contraction ratio, an aluminum honeycomb flow straightener, and two stainless steel turbulence reducing screens. The fan is driven by a 10hp AC motor and is oriented to pull the air down the tunnel. The operating range of the tunnel is 10mph ($4.5\frac{m}{s}$) to 145mph ($65\frac{m}{s}$). A photograph of the tunnel is shown in Figure 3.2.

The wind tunnel is controlled through the control panel located on the side of the tunnel, just downstream from the test section shown in Figure 3.3. Operation is initiated by first powering on the control panel followed by activating the start switch. Once power has been established, the airspeed indicator must be set to a positive number using the zeroing dial. When the indicator reads a positive number the fan can be engaged with the fan speed control. The indicator must be set to a positive number because a square root is used by the internal calculations of the airspeed indicator. If negative, the airspeed will not be calculated and the indicator will not change even though the fan begins to rotate. The airspeed indicator on the tunnel was used to establish reference points for multiple tests. The reference points were later verified for accuracy with a hot-wire CTA system.
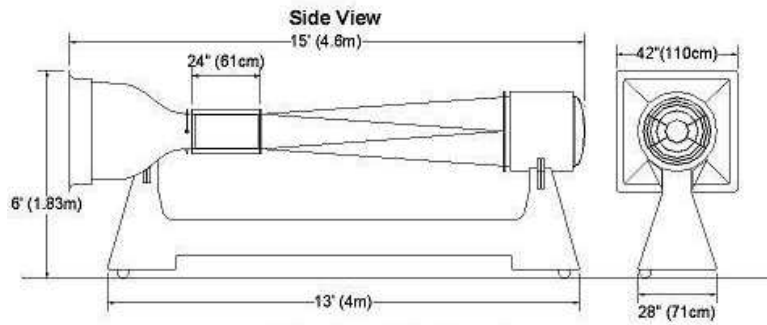

Figure 3.1:   Schematic of the Aerolab wind tunnel.
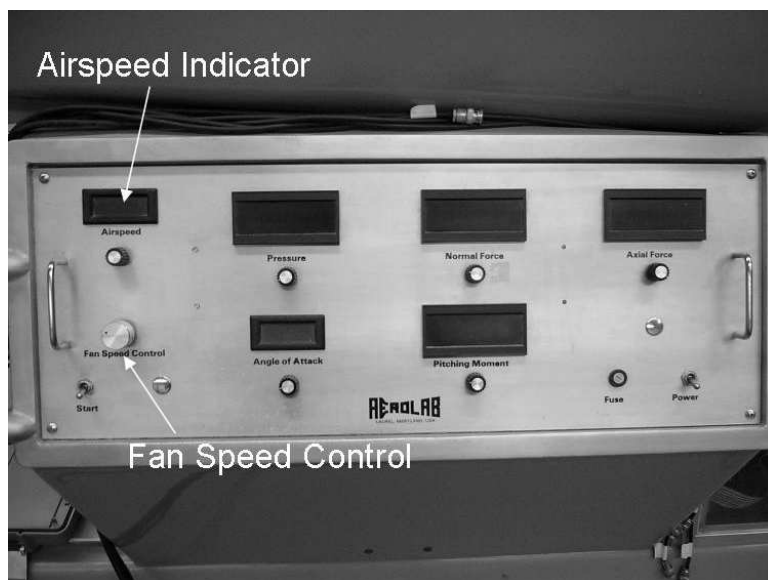
Figure 3.2:   Photograph of the Aerolab wind tunnel.

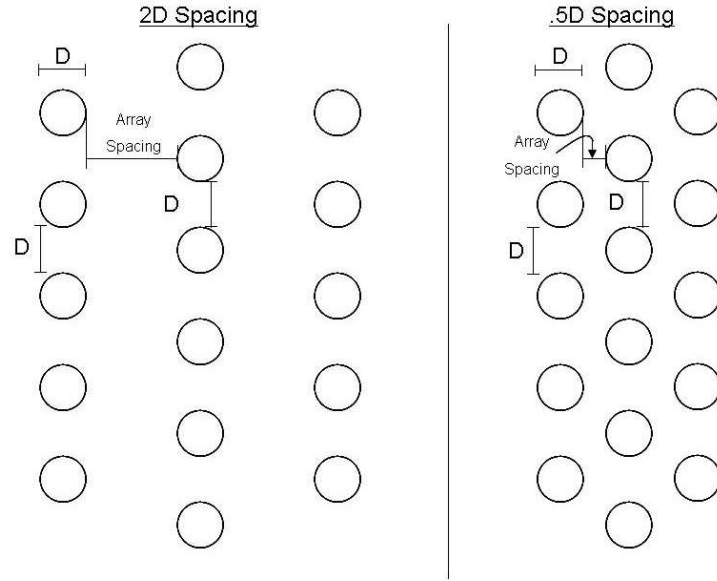Figure 3.3:   Photograph of the Aerolab wind tunnel control panel.

Figure 3.4:   Side views of cylinder arrays at 2D and 0.5D spacing.

3.2   Clutter Model

The cylinder arrays used to represent generic engine nacelle clutter are one half scale versions of the model used by Disimile et al. in their work involving the transport of water spray past generic clutter [11]. Each cylinder was 1 inch (25.4mm) in diameter. The model was constructed such that the three cylinder arrays and turbulence grid could all be mounted to a 0.25in (6.35mm) aluminum base plate and easily slid into the tunnel test section as one piece. The base plate was constructed to allow for the cylinder arrays to be placed at spacings of half the cylinder diameter, 0.5D, 1D, 1.5D, and 2D lengths. The spacing is measured from the furthest point back of the leading cylinder to the leading point of the consecutive cylinder as depicted in Figure 3.4.

Three cylinder arrays were constructed in coordination with the Air Force Institute of Technology, AFIT. The upstream most array contained five cylinders, the middle array held six, and the furthest array down stream had five. The cylinders in each array are offset from the array in front of it. Acrylic tubing was cut to lengths of 11.5in (292.1mm) to make the cylinders. This length is the width of the wind tun-
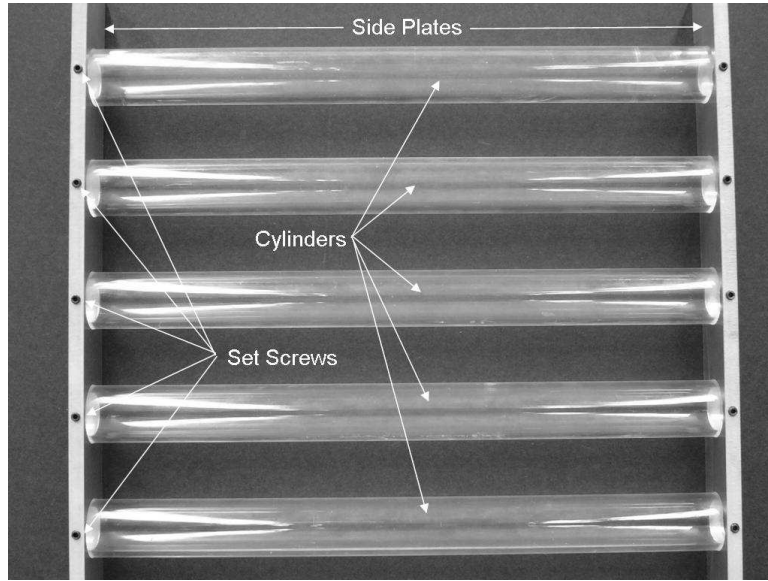
23

Figure 3.5:   Photograph of a five cylinder array.

nel test section once the side doors were closed and secured. Each array had 0.25in (6.35mm) aluminum plates on each side to hold the cylinders in place. Set screws were used to prevent the cylinders from rotating or sliding out of the side plates. Each side plate was then tapped at the bottom so they could be secured to the base plate. A five cylinder array can be seen in Figure 3.5.

The turbulence grid was made from a sheet of pre-manufactured steel screen. The screen was cut to the dimensions needed to fasten it to the base plate and fit inside the tunnel test section. It was cut large enough so that it could be wrapped around the leading edge of the base plate and be secured at the front as well as on the sides. By bending the grid at 90 degrees on both sides and securing it to the sides, the grid was made more rigid so it would not wobble in the flow of the wind tunnel. The dimensions of the screen openings were 0.5in (12.7mm) squares. The cross members of the mesh screen were 0.1875in (4.76mm). The dimensions can be seen in the schematic in Figure 3.6.

Figures 3.7 (a) and (b) show the entire assembly with all three cylinder arrays and the turbulence grid attached to the base plate. Figure 3.7 (a) shows the arrays

24
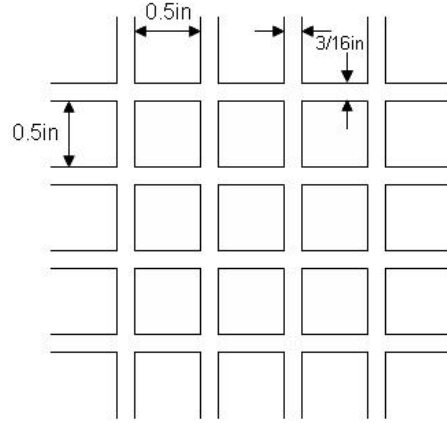
Figure 3.6:   Schematic of the turbulence generation grid.

| (a) | (b) |
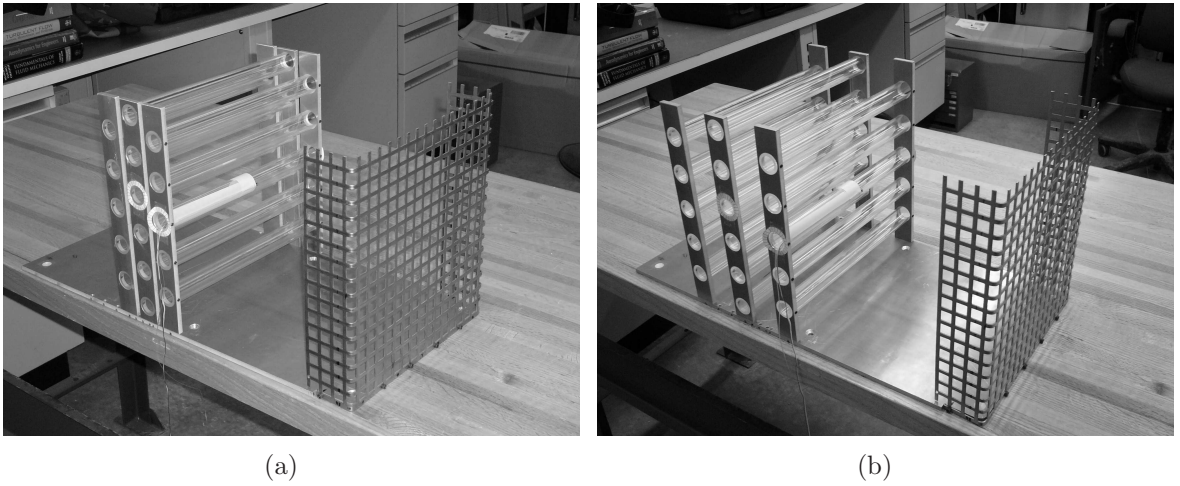
Figure 3.7:   Entire model assembly with cylinders arrays placed at (a) 0.5D and (b) 2D spacing.

at 0.5D spacing, while Figure 3.7 (b) shows the arrays at 2D spacing. Also, Figure 3.8 shows the entire model installed in the wind tunnel test section.

3.3   Instrumentation

A Constant Temperature Anemometry, CTA, hot-wire and a pressure trans-ducer were used to take data during this research. The pressure transducer was a 5 *psig* differential transducer. A pressure differential was measured with the reference pressure being the atmospheric pressure. The transducer was flush mounted to center
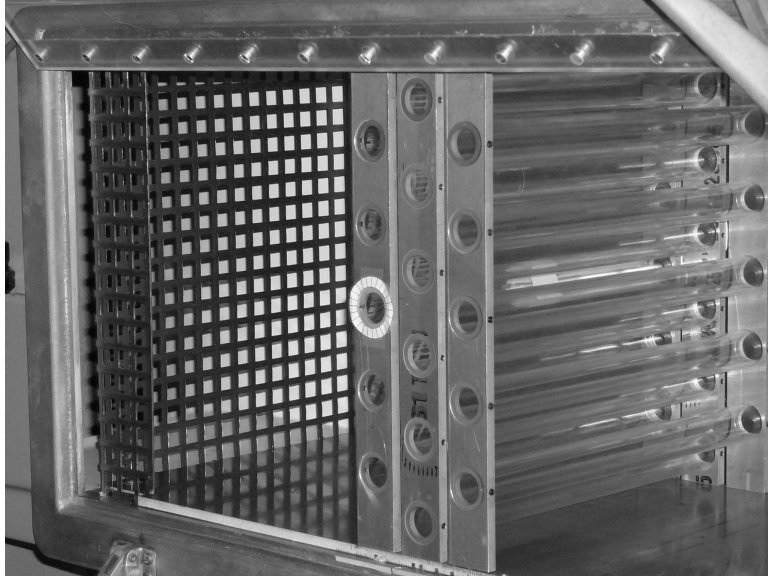
Figure 3.8: Photograph of entire model assembly installed in the wind tunnel test section. Shown with cylinder arrays at a 0.5D spacing, an upstream angle of view, and the turbulence grid in place.

cylinder on the array furthest upstream. The transducer's wires and a flexible tube securely attached to the reference pressure tap were inserted into the hollow cylinder and out the side door of the wind tunnel. A photograph of the pressure transducer while mounted to the front-center cylinder can be seen in Figure 3.9.

Mean pressure data was taken from the pressure transducer using an Endevco 4428A pressure signal indicator. The transducer and the pressure indicator were calibrated together to determine the millivolt, mV, output per psi. Millivolt readings were taken from the pressure indicator, recorded and converted to pressure in psi using the calibration curve fit.

Along with mean pressure, a Hewlett Packard HO35670A dynamic spectrum analyzer was used to measure fluctuation response of the pressure transducer. Wakes shed from the cylinders at a specific rate based on the free-stream velocity of the flow. This shedding caused a fluctuation in the pressure transducer readings. While a mean pressure value was taken from the signal indicator, the average value of the fluctuations were obtained by the dynamic analyzer. The frequency of the pressure

Figure 3.9:   Photograph of the 5psig pressure transducer flush mounted to the front-center cylinder.

fluctuations were taken in terms of a root mean squared, RMS, value. The RMS value provides the average magnitude of the pressure variations. This analysis will offer insight to the rate at which the wakes are shedding off the cylinder.

The hot-wire CTA probe used was a Dantec 55P91 three-wire probe. The probe arm was mounted to an Aerotech 3-D traverse system and inserted into the test section through a slotted window on the top of the wind tunnel. The traverse allowed for the probe arm to be positioned at any vertical, horizontal, or stream-wise position accessible through the slot in the ceiling window. Once stationary, the hot-wire took velocity data in the test section. Since a three-wire probe was used, velocity components in all three directions could be obtained. A sketch and photograph of the hot-wire probe can be seen in Figure 3.10.
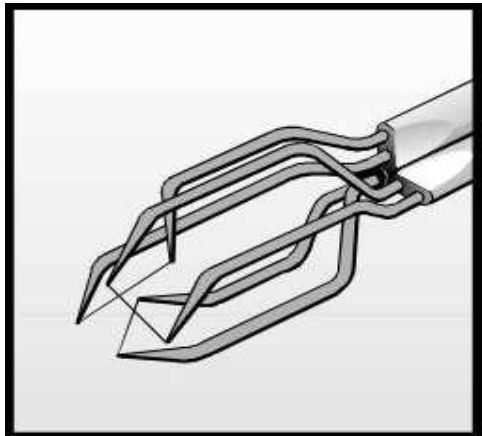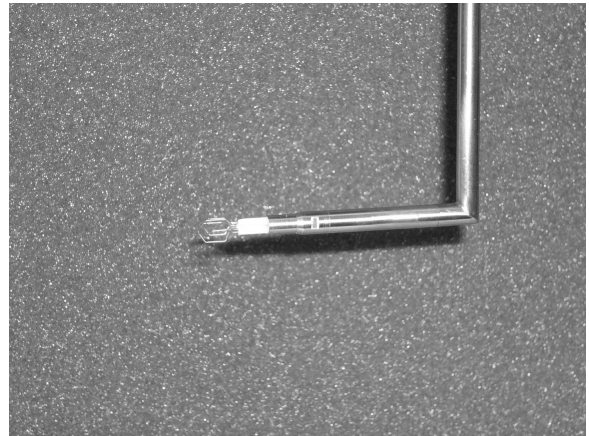
| (a) | (b) |

Figure 3.10:   3-wire hot-wire probe (a) sketch and (b) photograph.

IV. Results and Analysis

A large amount of research has been done on single cylinders as well as staggered cylinder bundles. The focus has been on incoming laminar flow and the turbulent wake produced by the cylinder. However, the flow inside of an engine nacelle is turbulent before it impinges on obstructions. The focus of this research is to make a comparison between incoming turbulent and laminar flow to see if the difference has an effect on the wake regions of a single cylinder and staggered cylinder arrays. This comparison will provide insight into easier methods of predicting turbulent airflow propagation through a cluttered engine nacelle.

4.1 Hotwire Analysis

Hot-wire data was collected using a StreamLine Constant Temperature Anemometry (CTA) System by Dantec Dynamics. A three-wire hot-wire probe was used to collect velocity data inside the wind tunnel test section. The CTA system collected and recorded data in the form of voltage differentials across the probe wires. This voltage was then converted to component velocities as described in Chapter II. Mean velocities and root mean square (RMS) values for each component were collected at each data point. The RMS values are the velocity perturbations of their respective component.

4.1.1 Turbulence Intensity. In order to quantify the turbulence intensity (TI), velocity data was collected 9 diameters [i.e. 9in (228.6mm)] downstream from the location of the turbulence grid along the tunnel centerline. This location was selected to obtain the TI of the airflow as it approached the cylinder arrays. TI was obtained with and without the grid for a range of speeds.

The wind tunnel airspeed indicator on the control panel was used as a reference between different test configurations. This airspeed was calculated using pressure ports located just in front of the test section. This location was 2.5in (63.5mm) upstream of the turbulence grid. The precision of the wind tunnel was assumed to

Table 4.1: Airspeed and Turbulence Intensity without a Turbulence Generation Grid.

Tunnel Indicated Airspeed mph ($\frac{m}{s}$)	Hot-wire U_{Mean} Velocity mph ($\frac{m}{s}$)	%TI
11.2 (5)	9.78 (4.4)	0.85
22.4 (10)	22.7 (10.16)	0.66
40 (17.88)	42.4 (18.9)	0.59
60 (26.8)	66 (29.5)	0.53

be correct, however the accuracy was unknown. In other words, it was assumed that matching indicated airspeeds during different tests resulted in the same airflow velocity. However, it was not known if the control panel's indicated airspeed, based on the differential pressure input, was correct. Velocities are reported as tunnel indicated speeds. These speeds can be used as reference points and then correlated back to the hot-wire measured speed. The hot-wire was calibrated and known to be accurate. Due to the fact that the tunnel's indicated speed was measured before the turbulence grid, if installed, and the hot-wire measurements were taken downstream of the grid location, slight discrepancies between the two may exist. By referencing the tunnel indicated speeds to the hot-wire speeds, commonality existed between the various tests with and without the turbulence grid.

Table 4.1 shows the control panel indicated speed, the streamwise component of the hot-wire speed and the TI when no turbulence grid was installed. Table 4.2 shows the same information with the turbulence grid in place. A tunnel indicated speed of 52mph ($23.2\frac{m}{s}$) was used with the grid instead of 60mph ($26.8\frac{m}{s}$) due to the fact that this was an operability limit reached by the tunnel with the grid obstructing the test section. A TI of 6-7% was created with the turbulence generation grid.

4.1.2 Vertical Traverse. Data through a vertical traverse was taken behind the cylinder arrays. This was done to quantify the mean component velocities and the turbulence intensities downstream of the clutter. A test matrix for the vertical traverse is shown in Table 4.3. The 0.5D spacing for the three cylinder arrays was chosen due to size constraints of the wind tunnel. The probe location during this test

Table 4.2:   Airspeed and Turbulence Intensity with a Turbulence Generation Grid.

Tunnel Indicated Airspeed mph ($\frac{m}{s}$)	Hot-wire U_{Mean} Velocity mph ($\frac{m}{s}$)	%TI
11.2 (5)	9.8 (4.4)	6.12
22.4 (10)	20.6 (9.2)	6.78
40 (17.88)	38.8 (17.3)	6.78
52 (23.25)	51.2 (22.9)	6.91

was centered horizontally and was 2in (50.8mm) down stream of the trailing edge of the furthest downstream tube(s). The vertical traverse data was taken every 2mm over a range of +20mm to -20mm from the centerline of the center tube. This also corresponds to the center line of the tunnel. The data sampling rate at each location was 5 kHz for 1 second. Data was collected for all four configurations with the tunnel indicated airspeed set to 30mph ($13.4\frac{m}{s}$). Extrapolated from the turbulence intensity data, this would indicate that the test section airspeed entering the model was 31.2mph ($13.9\frac{m}{s}$) when no turbulence grid was present and 28.4mph ($12.7\frac{m}{s}$) when the turbulence grid was present. These values are close enough to allow a valid comparison between grid and no-grid effects. A more comprehensive extrapolation between control panel indicated airspeeds and hot-wire measured air speeds can be found in Appendix A.

Reynolds number is a value based on airflow past one cylinder and does not include the presence of multiple cylinders when calculated. However, for the purposes of this study, the Reynolds number was calculated, using Equation 2.1, for each case in terms of one cylinder. Since all of the tubes used were the same size, this at least allows for a comparison point among other experiments. For the vertical traverse data collection, Re was calculated to be approximately 24,000. This was based off a 1in (25.4mm) diameter, 30mph ($13.4\frac{m}{s}$) airflow, ρ at $1.229\frac{kg}{m^3}$, and a μ of $1.73\text{x}10^{-5}\frac{N-s}{m^2}$.

Figure 4.1 shows the turbulence intensities across the traverse for the four cases. For the cases with 3 arrays, it can be seen that TI stays within a 5-7% range across the length of the traverse. While the intensity begins to dip while the traverse is above

Table 4.3:   Vertical Traverse Test Matrix.

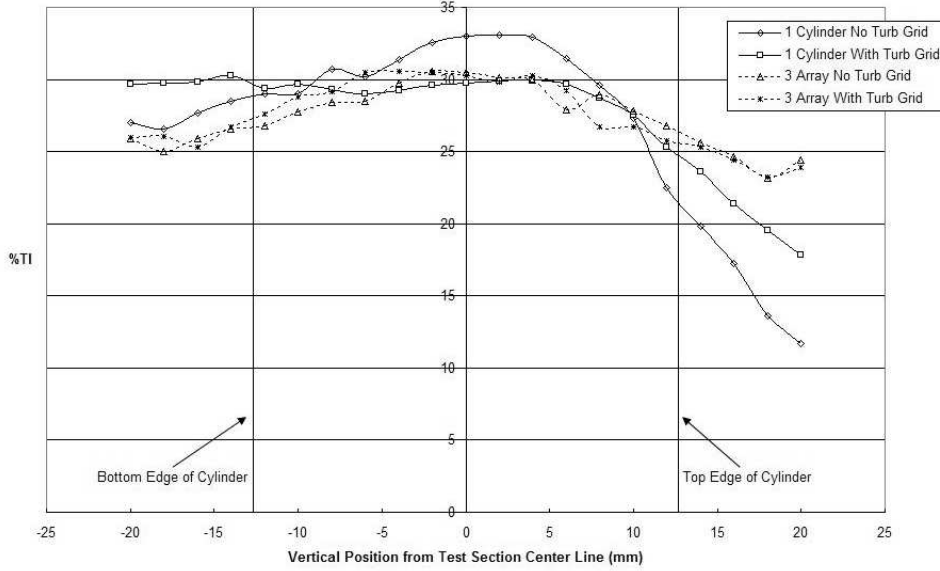| 1 Cylinder	1 Cylinder
No Turbulence Grid	With Turbulence Grid
3 Cylinder Arrays 0.5D Spacing No Turbulence Grid	3 Cylinder Arrays 0.5D Spacing With Turbulence Grid

Figure 4.1:   Turbulence Intensity across a range of -20mm to +20mm from the center line of the cylinder array model.

the cylinder, TI levels still remain in the 25-30% range. As expected, the intensity is highest behind the cylinder, but overall change is low. On the other hand, the TI for both single cylinder cases stays with the same 5-7% range until the top edge of the cylinder is reached. Here it begins to fall significantly. For three of the configurations, maximum turbulence intensities occur behind the profile of the cylinder. This result shows that the streamwise momentum of the airflow above the cylinder dominates the profile of the airflow.

Other than the single cylinder case with a grid, these maximums all occur less than 5mm from the center of the tube. The outlier point from the single cylinder with a grid case, as well as the asymmetric drop offs above and below the cylinder will be discussed towards the end of this section.
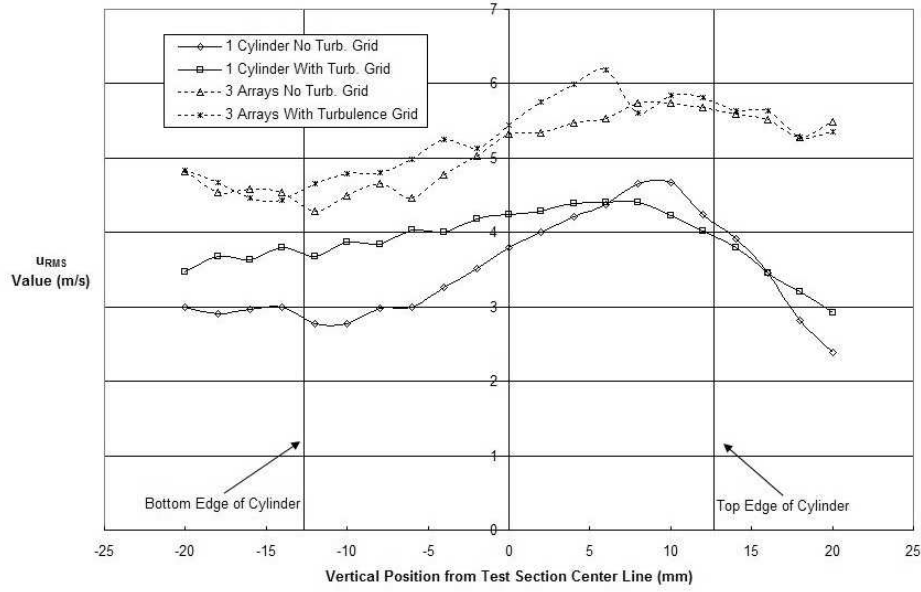
Figure 4.2: Velocity Perturbation across a range of -20mm to +20mm from the center line of the cylinder array model.

The airflow perturbations see the same general trend as the TI. Peak values occur within the profile of the cylinder, a more significant drop off is seen above the cylinder, and all perturbation magnitudes stay within a small range, about $2\frac{m}{s}$ from the min to the max. In Figure 4.2 it can be seen that each configuration follows the same pattern. However, the 3 array cases, with more obstructions present, produced perturbations of higher magnitude. Again, an asymmetric pattern has formed.

Figure 4.3 shows the mean velocity of the streamwise component of the airflow past the model configurations. Mean values were calculated form the 5,000 samples taken at each location. For all cases, except the one cylinder with a grid configuration, the lowest value occurs behind the profile of the cylinder. For the single cylinder, with grid case, the lowest value was below the edge of the cylinder.

The lowest velocities are expected in this region, however they are expected to be closer to the centerline of the cylinder, especially for the single cylinder configuration with no grid. As with the perturbations, the mean streamwise velocity of the 3 array configurations has a higher magnitude than the single cylinder cases. The hypothesis
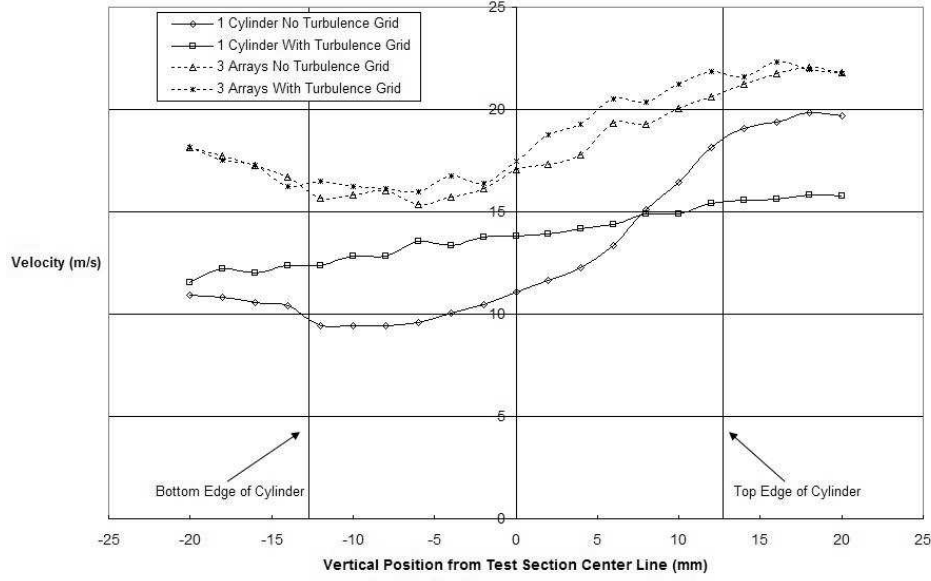
33

Figure 4.3: Mean Horizontal Component Velocity across a range of -20mm to +20mm from the center line of the cylinder array model.

for this result is that the additional blockage present with 3 arrays is causing the velocity of the airflow passing between the cylinders to be greater.

At roughly 30mph ($13.4\frac{m}{s}$), Re approximately 24,000, very similar trends take place between the different model configurations. For the most part, turbulence intensity and perturbations are highest while streamwise mean velocity are lowest behind the cylinder profile. High perturbations and TI along with lower velocities behind the cylinders indicate higher mixing, a condition inherent to a recirculation zone, as discussed in Chapter II.

However, there are two cases that present interesting results. One is the asymmetric patterns of these parameters and the second is the outlier data points associated with the single cylinder case with a turbulence grid. In this case, the highest turbulence was below the cylinder while the lowest streamwise mean velocity was above the cylinder. At this time, the trend is inconclusive and is a subject for further investigation. Further investigation into this condition should answer whether this is

Table 4.4:   Vertical Traverse Location of Min and Max Value.

	TI Highest Value z location (mm)	u_{RMS} Highest Value z location (mm)	U_{Mean} Lowest Value z location (mm)
1 Cyl, w/o Grid	4	10	-12
1 Cyl, w/ Grid	-14	8	-20
3 Arrays, w/o Grid	-2	8	-6
3 Arrays, w/ Grid	-4	6	-6

an occurring phenomenon, or if this result came about due to an outside influence during testing.

The asymmetry about the centerline of the cylinder was seen in all test configurations. For the single cylinder case with no turbulence grid, it is expected that the highest turbulence intensities, highest perturbations, and lowest horizontal mean velocities would be seen at the center line behind the cylinder. However, these patterns did not happen for the single cylinder case with no turbulence grid, nor any of the other three cases. Unfortunately no distinctive pattern was seen. Table 4.4 shows the location where each min or max value occurred for each of the configurations.

As mentioned above, certain aspects are expected with the single cylinder case when a turbulence grid is not present. For example, the velocity profile for the wake behind a symmetric blunt body should have minimum flows along the centerline and be symmetric about centerline. The theoretical profile of the average velocity at the downstream location of the airflow can be calculated using Equation 4.1 [22].

$$\bar{u} = U - \Delta u \tag{4.1}$$

In Equation 4.1, $\bar{u}$ is the average velocity at the location downstream of the cylinder, U is the freestream velocity, and Δu is the velocity difference. According to White, the solution for the theoretical wake profile behind a cylinder was presented in a dissertation by H. Schlicting in 1930. This profile, characterized by Δu, is calculated using Equation 4.2.

$$\Delta u = \Delta u_{max} \left[1 - \left(\frac{y}{b} \right)^{\frac{3}{2}} \right]^2 \tag{4.2}$$

Here Δu_{max} is the maximum velocity difference experienced downstream of the cylinder, y is the vertical location and b is growth parameter of the wake. The growth parameter, b, is a finite value related to drag obtained from theory [22]. It can be calculated with the cylinder diameter, D, the downstream distance from the cylinder, x, and the coefficient of drag C_d using Equation 4.3

$$b \approx 0.576 \sqrt{C_d x D} \tag{4.3}$$

The coefficient of drag for this case was taken from a correlation in White [22] that related Reynolds number to C_d. For a Reynolds number of approximately 24,000, C_d was on the order of 1. With all of these parameters, Δu_{max} can be found using Equation 4.4.

$$\Delta u_{max} \approx 0.98 \left(\frac{C_d D}{x} \right)^{\frac{1}{2}} \tag{4.4}$$

A comparison of the theoretical wake velocity and the experimental data from the one cylinder, no grid case can be seen in Figure 4.4. In this case, the experimental data is close, but slightly askew. It can be seen that a trend is forming that makes sense, however, the experimental data does not show similar magnitudes of velocity below the cylinder as it does above.

The asymmetric patterns could be a phenomenon of the flow field around the cylinders. However, since it is occurring in instances when known profiles are historically established, this is unlikely. A more likely cause for the asymmetric pattern is the proximity of the hot-wire probe to the cylinder. At 2 inches downstream, the probe is within the recirculation zone of the cylinder wake. This location was selected because the recirculation zone was a region of interest for flow characterization.
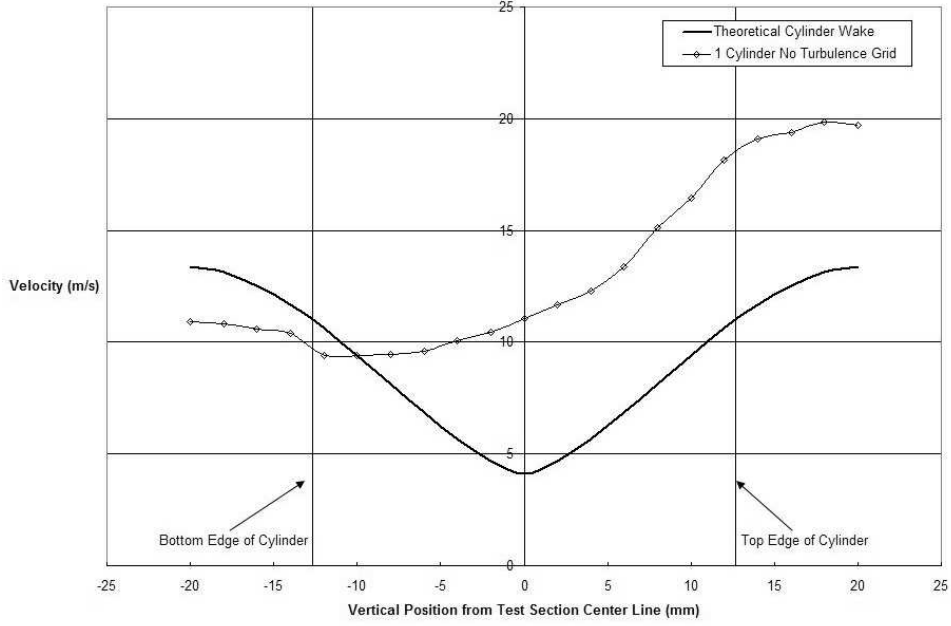
Figure 4.4:   A comparison a theoretical wake velocity profile and the streamwise mean velocity collected 1 cylinder with no turbulence grid.

Upon further research of the capability of the hot-wire, it was found that the hot-wire has an operating region represented by a 70° cone around the probe [9]. This indicates an inability of the hit-wire to differentiate between positive or negative streamwise flow directions. By calculating negative velocities as positive, the calculated average velocity will become higher. This could be the cause of the asymmetric pattern occurring in the vertical traverse. Higher average velocities seen in Figure 4.3 could be the result of hot-wire producing averages higher than what exists.

Select points along the vertical traverse of the one cylinder case with no turbulence grid were repeated to compare to the original results. These points showed repeatability and eliminated the possibility of tunnel and model configuration misalignments. This places more emphasis on the hot-wire reverse flow inability as to being the cause of the asymmetric patterns.

No patterns were seen in the location of the minimum and maximum values for U_{Mean}, u_{RMS}, and TI. This indicates that this phenomenon was not caused by the probe being misaligned in the test section. If the probe was not centered properly on

37

the model or if it was not mounted perfectly horizontal in the test section, the min and max values should all be shifted in the same direction.

Another possible reason for the resultant flow characteristic is that there are access channels running in the window ceiling of the test section. These were taped off during testing, however space was left untaped for the hot-wire probe mounting arm to be inserted into the wind tunnel. Untaped sections were kept to a minimum, but, leakage would still have occurred. This leakage could cause flow angularities to occur due to suction at the top of the test section. These angularities could effect the flow patterns around the cylinder model configurations. Further investigation into this matter could be explored by bringing the probe in from either the side walls or the floor of the test section and seeing if similar phenomenon develop.

Even though there is a bit of discrepancy in the location of minimum and maximum values, as well as the presence of an asymmetry, general trends were still present in the vertical traverse data. Most min and max values occurred within the edges of the cylinder. This suggests that the effect of upstream turbulence is negligible when making first order approximations of airflow past engine nacelle clutter.

4.2 Differential Pressure Analysis

Differential pressure data was taken using a LQ-125-5D Kulite Semiconductor Products, Inc. $5psi$ pressure transducer. The pressure transducer was flush mounted to the outside surface of the center cylinder in the upstream most array. The leading edge of the upstream most array was 10.5 diameters [10.5in (266.7mm)] from the turbulence grid. Mean pressure was taken for every test point. Likewise spectral analysis of the pressure fluctuations were also taken at various points. Data points were collected at 15° increments along the top circumference of the cylinder from the leading edge to the trailing edge, 0° to 180°.

4.2.1 Mean Pressure. Mean Pressure was taken for five model configurations, each with and with out the turbulence generation grid. The test matrix of the

Table 4.5:   Mean Pressure Test Matrix.

1 Cylinder No Turbulence Grid	1 Cylinder With Turbulence Grid
1 Cylinder Array No Turbulence Grid	1 Cylinder Array With Turbulence Grid
2 Cylinder Arrays 0.5D Spacing No Turbulence Grid	2 Cylinder Arrays 0.5D Spacing With Turbulence Grid
3 Cylinder Arrays 0.5D Spacing No Turbulence Grid	3 Cylinder Arrays 0.5D Spacing With Turbulence Grid
3 Cylinder Arrays 2D Spacing No Turbulence Grid	3 Cylinder Arrays 2D Spacing With Turbulence Grid

configurations can be seen in Table 4.5. Once the pressure differentials were tabulated, the coefficient of pressure, C_P, was calculated and plotted over the range of the top hemisphere of the cylinder. An atmospheric pressure was used as the reference pressure with the transducer. Because of this, C_P should be considered an atmospheric reference C_P instead of a traditional C_P.

It is important to spend time visiting the use of atmospheric pressure as the reference pressure. The coefficient of pressure is a measure used to non-dimensionalize the local static pressure about a surface. For most cases, using the atmospheric pressure as a static reference is justified since most wind tunnels are designed with very low losses as the airflow enters the test section. In the case of this research an extremely intrusive obstruction was added to the flow, in the form of the turbulence grid. There is a significant total pressure loss as flow crosses the turbulence grid [4]. Total pressure is the sum of static pressure and dynamic pressure. Since the velocity is maintained through the grid the dynamic pressure is unchanged. To compensate, static pressure is significantly lower in the test section when the grid is installed. This difference in reference static pressure is the cause of all the turbulent grid C_P's starting at a -1 value. Traditionally, C_P should always start at 1. This is why all C_P values contained within this document are considered atmospheric reference C_P's.
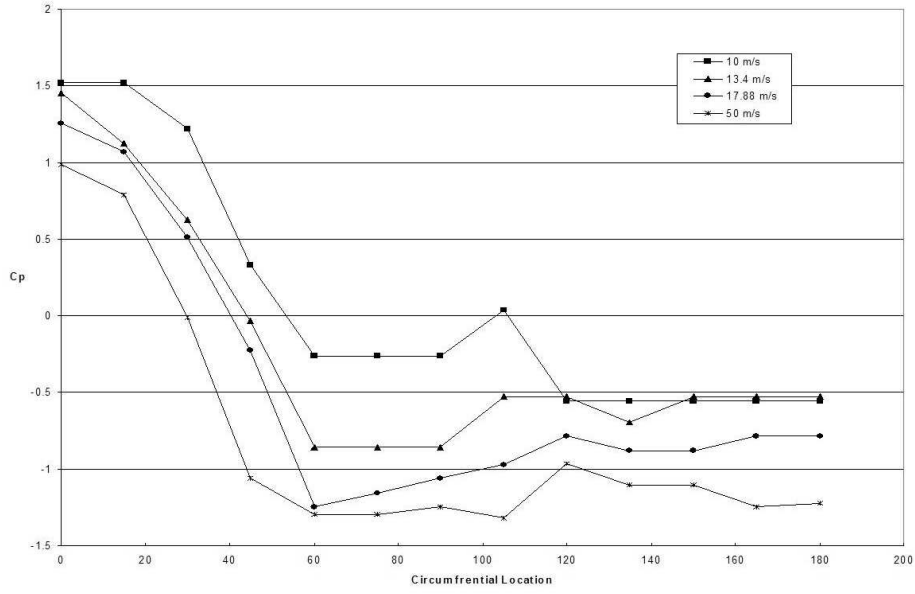
Figure 4.5: C_P at 15° increments across the top of 1 cylinder without turbulence generation grid installed.

As a baseline, pressure measurements were first taken for a single cylinder. Figure 4.5 shows the C_P distribution across the cylinder. The data presented in Figure 4.5 is consistent with historical trends of experimental measurements of C_P. At the 0° location, C_P is at or around 1. It drops off as the location angle increases until it reaches a minimum close to the 90° point. From here it begins to increase until the separation point is reached, at which point C_P levels off. the leveling off of C_P on the downstream side of the cylinder is due to the pressure transducer entering the wake region where a recirculation region exists.

Along with a single cylinder with no turbulence grid, data was collected for the single cylinder with the grid installed. It can be seen in Figure 4.6 that the turbulence grid does not affect the trend of C_P around the upper circumference of the cylinder. Combining Figures 4.5 and 4.6 into Figure 4.7 shows the only effect the turbulence grid has on the pressure around the cylinder is magnitude of the pressure drop.

New trends emerge when the first array is installed. At the 90° point instead of raising and leveling off, C_P experiences an initial rise, then falls off again before
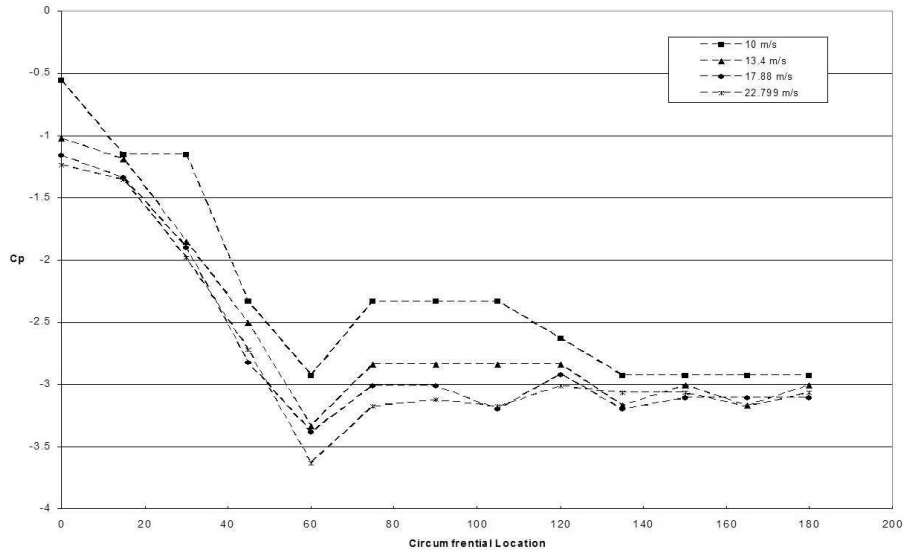
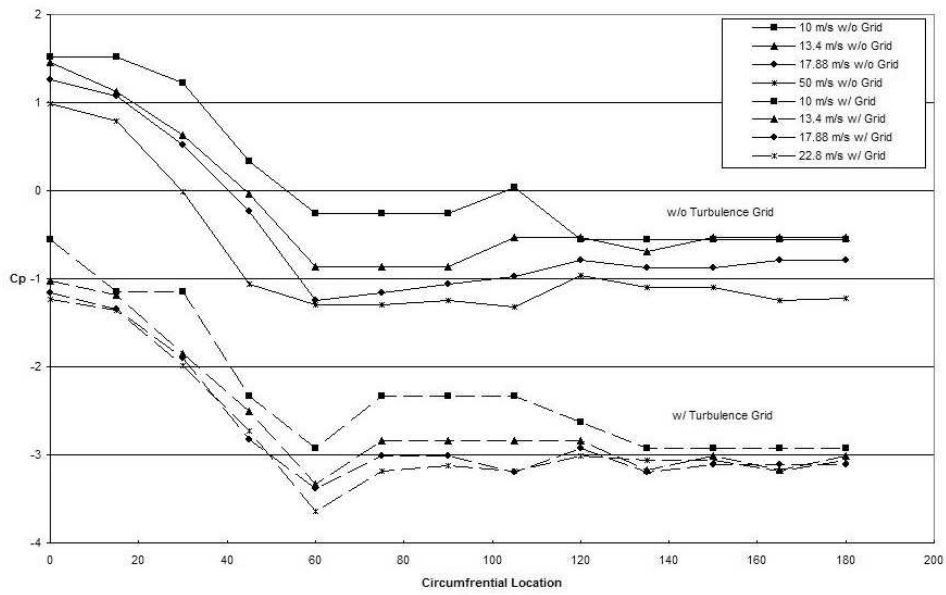Figure 4.6: C_P at 15° increments across the top of 1 cylinder with a turbulence generation grid installed.

Figure 4.7: C_P at 15° increments across the top of 1 cylinder with and without a turbulence generation grid installed.
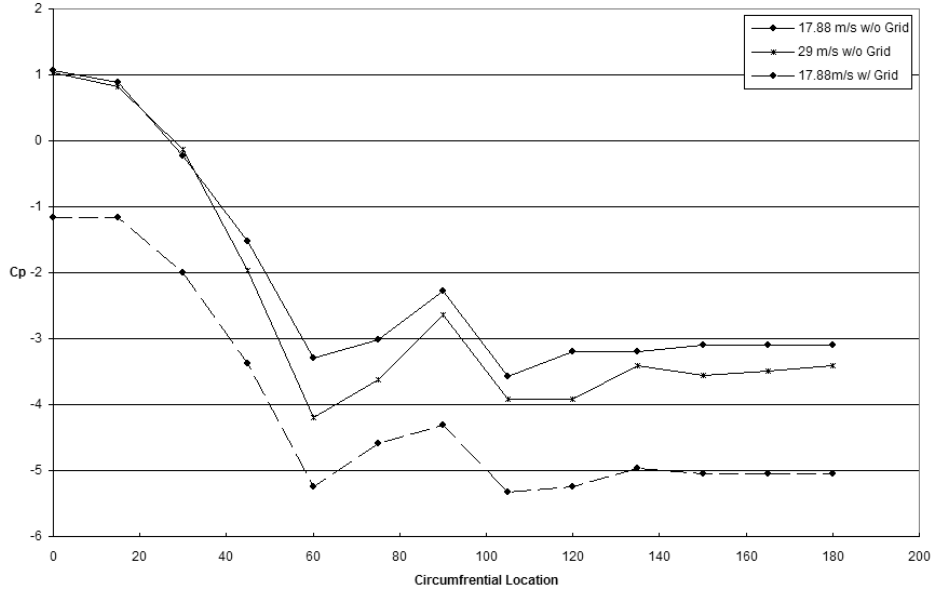
Figure 4.8: C_P at 15° increments across the top of 1 cylinder in a full array with and without a turbulence generation grid installed.

leveling out past the separation point. This is shown in Figure 4.8. Also, the magnitude of the pressure differential is greater than the single cylinder case. This is most likely due to an increase in the velocity of the airflow passing in between two adjacent cylinders. This increase in velocity is due to the fact there is more blockage in the test section. This phenomenon is why 40mph $(17.88\frac{m}{s})$ and 65mph $(29\frac{m}{s})$ were chosen as speeds to collect data. The maximum achievable wind tunnel speed with the turbulence grid and one array in place was 40mph. Likewise, 65mph was the maximum wind tunnel speed with only the single array installed. Both of these velocities were a result of the blockage in the tunnel. Again, it is important to note here that these speeds are the speeds of the tunnel's control panel airspeed indicator.

Similar to one full array, when the second and third arrays are added, a spike followed by a drop off in mean pressure occurs after the separation point. As seen in Figure 4.9, this effect is not as pronounced as the case with only one full array. This indicates that the effect of the added blockage increases the airspeed in between adjacent cylinders. However, it is obvious that an effect is now also being experienced
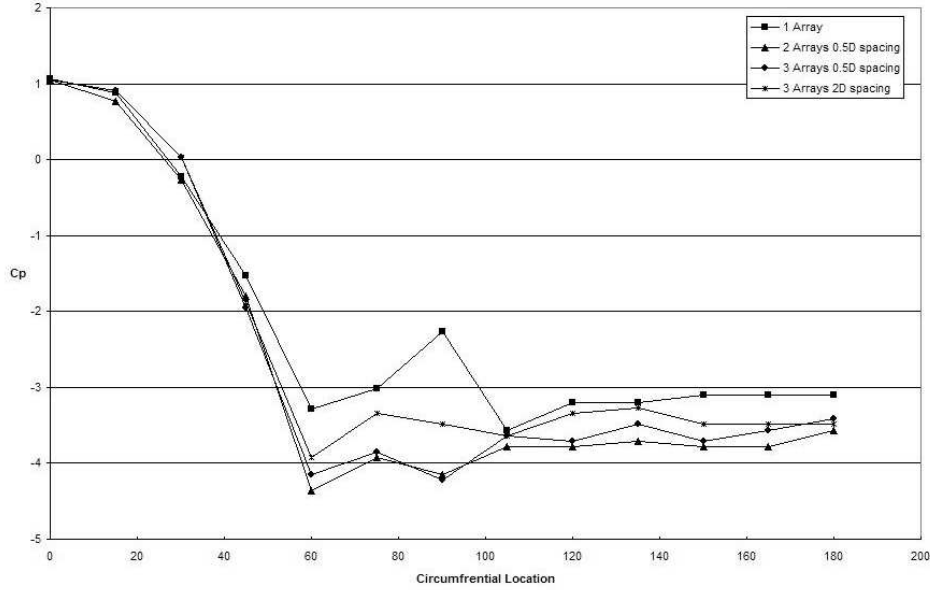
42

Figure 4.9: C_P at 15° increments across the top of 1 cylinder in 1, 2, and 3 full arrays without a turbulence generation grid installed and airflow at $20\frac{m}{s}$.

from the downstream arrays. From Figure 4.9 it can be seen that the highest to lowest speeds between the cylinders are experienced in this order:

1. 2 Arrays, 0.5D spacing between arrays

2. 3 Arrays, 0.5D spacing between arrays

3. 3 Arrays, 2D spacing between arrays

4. 1 Array

While added blockage does increase airspeeds in between cylinders, a point is reached when enough blockage begins to decrease that flow. However, if spacing is increased as blockage is added, velocities gradually decrease and the pressure spike around the separation point is less intense.

The addition of the turbulence generation grid produces the same general trends as when the grid is not present. Seen in Figure 4.10, the magnitude of the pressure drop around the circumference of the cylinder is the same as the uninstalled grid case. Likewise, the magnitude of the pressure spike and drop off around the separation point
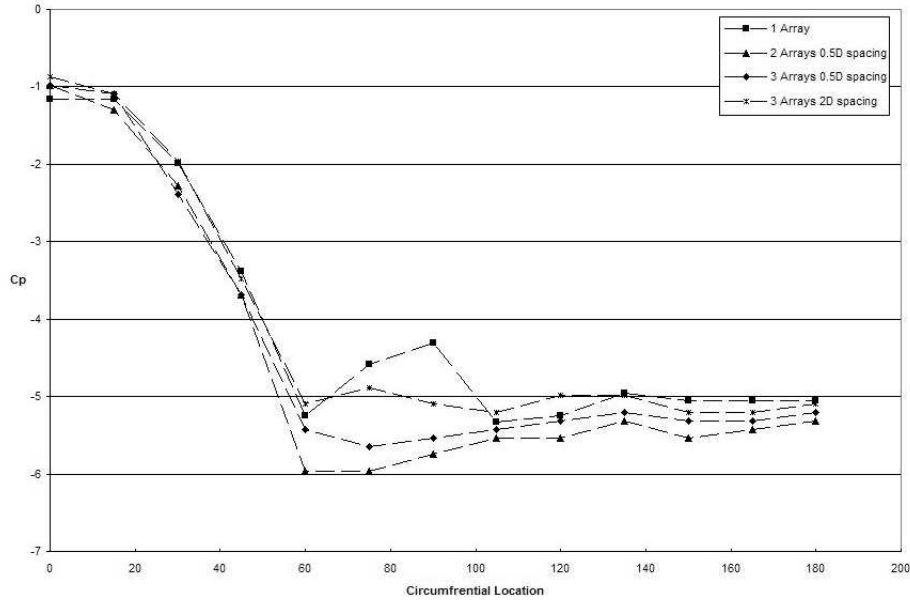
43

Figure 4.10: C_P at 15° increments across the top of 1 cylinder in 1, 2, and 3 full arrays with a turbulence generation grid installed and airflow at 16.5 $\frac{m}{s}$.

is similar to the grid-less case. However, due to turbulent air upstream of the clutter, initial pressures at the front of the cylinder are lower.

4.2.2 Pressure Fluctuation Dynamic Response.   During the collection of pressure differential data, frequency response was also monitored at several locations around the cylinder and at several speeds. Frequency response was monitored by sending the signal from the pressure transducer to a dynamic signal analyzer. The analyzer was then able to display millivolt, mV, peak values by taking time averaged measurements. The average mV RMS values were displayed against the frequency at which they occurred. From the frequency at which these peaks occurred Strouhal, St, numbers were calculated. The Strouhal number is a non-dimensional number that characterizes the vortex shedding frequency of the cylinder and is defined in Equation 4.5 where f is the vortex shedding frequency, D is the diameter of the cylinder, and U is the airspeed as it approached the cylinder(s).
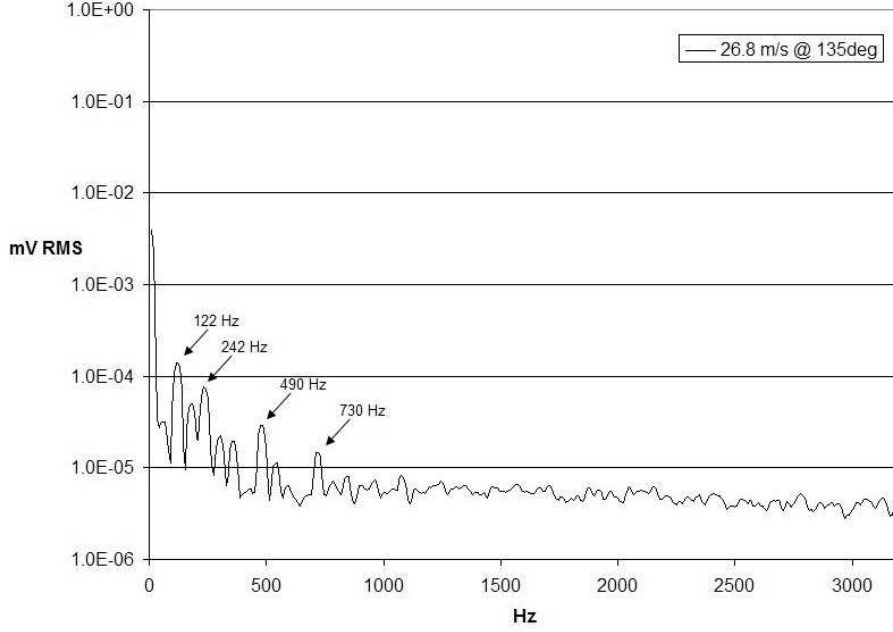
44

Figure 4.11:   Pressure frequency response of 1 cylinder at the 135° point in 26.8 $\frac{m}{s}$ tunnel indicated flow with no turbulence grid installed.

$$St = \frac{fD}{U} \qquad (4.5)$$

At lower speeds, $10\frac{m}{s}$ and below, it was difficult to distinguish between actual response and noise in the signal. Definitive peaks began to emerge at higher speeds. Luckily, frequencies began to repeat between different test configurations. This showed similarities exist between test cases.

Initially, as with the mean pressure measurements, initial investigations were done with a single cylinder without a turbulence generation grid. Figure 4.11 shows the frequency response taken from the signal analyzer for a 1 cylinder case with no turbulence grid in place with the tunnel airspeed indicator reading 60mph (26.8 $\frac{m}{s}$). Peaks begin to develop at the 135° location on the cylinder. These peaks are not as definitive as will be seen in later cases, but distinguishable frequencies were obtained.

Increasing the tunnel indicated airspeed to 110mph ($49\frac{m}{s}$) caused very definitive peaks occur around $430Hz$ and $860Hz$. This is seen in Figure 4.12. Here, when the
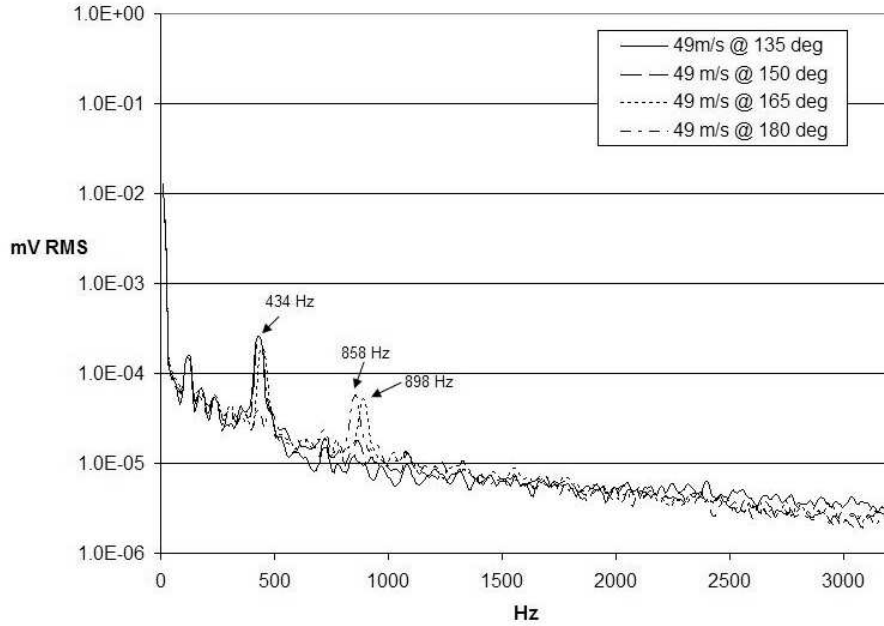
45

Figure 4.12:   Pressure frequency response of 1 cylinder from 135° to 180° in 49 $\frac{m}{s}$ tunnel indicated flow with no turbulence grid installed.

speed is doubled, the frequency response doubles. Since frequency is divided by velocity when calculating St, this indicates that St will remain the same as the lower speed. Establishing a matching Strouhal number raises the level of confidence of the test results.

Adding the turbulence generation grid with an airflow closer to that of Figure 4.11, in this case 51mph $\left(22.8\frac{m}{s}\right)$ due to the additional obstruction, more definitive peaks are seen. Shown in Figure 4.13. The magnitude of the response peaks is not as high, but more clear peaks develop.

Further increasing the clutter to 1 array full of five cylinders showed an increase in the predominant frequency of the vortex shedding. This is seen in Figure 4.14. While a predominant peak appears around a frequency of $586Hz$, subtle peaks can be seen in the range of $250\text{-}300Hz$. This would indicate that a shedding frequency similar to the single cylinder case is present, but is being masked by other factors.
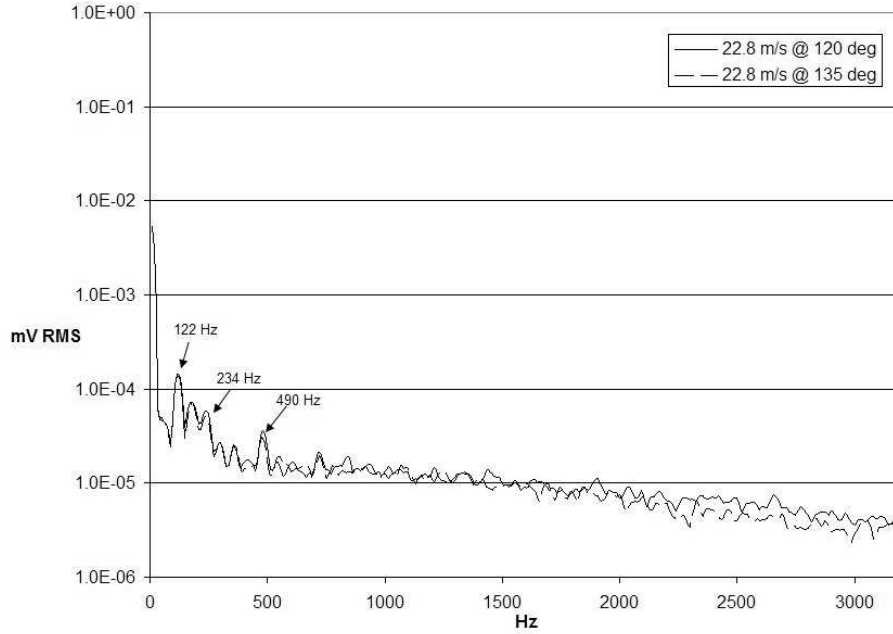
46

Figure 4.13: Pressure frequency response of 1 cylinder from 120° to 135° in 22.8 $\frac{m}{s}$ tunnel indicated flow with a turbulence grid installed.

These factors may include, signal noise, tunnel vibrations during testing, or even other circulation phenomenon coming from smaller eddies within the bulk vortex shedding.

Adding the turbulence grid to the single full array produced frequency responses similar to the single cylinder case. The wind tunnel indicated airspeed was less due to more blockage in the test section, but the same frequencies were obtained. This result, seen in Figure 4.15 shows the pattern start to develop between clutter configurations.

Increasing the clutter to two and three full arrays shows that similar patterns continue to persist. Figure 4.16 shows response peaks occur at $266Hz$ and $690Hz$ with no turbulence grid installed. Likewise, with the turbulence grid installed, responses can be seen at $202Hz$ and $354Hz$ in Figure 4.17. While these numbers vary slightly from those seen with one array or one cylinder, they are still in a similar range. This, along with the definitive separation between peeks shows a distinct shedding. The lower frequencies experienced when the turbulence grid installed could be a result of the slower tunnel indicated speed with more clutter present.
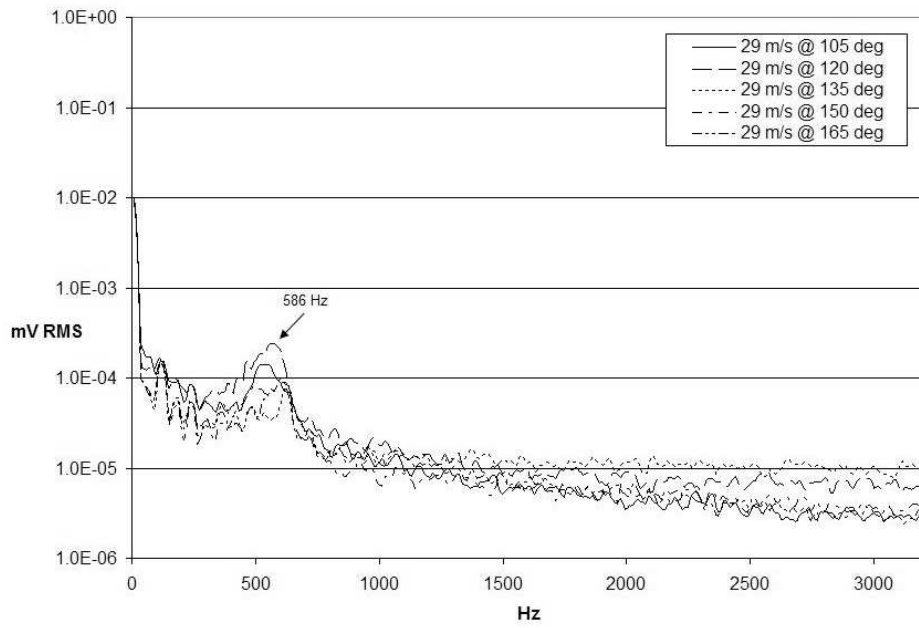
47

Figure 4.14: Pressure frequency response of 1 five cylinder array from 105° to 165° in 29 $\frac{m}{s}$ tunnel indicated flow with no turbulence grid installed.
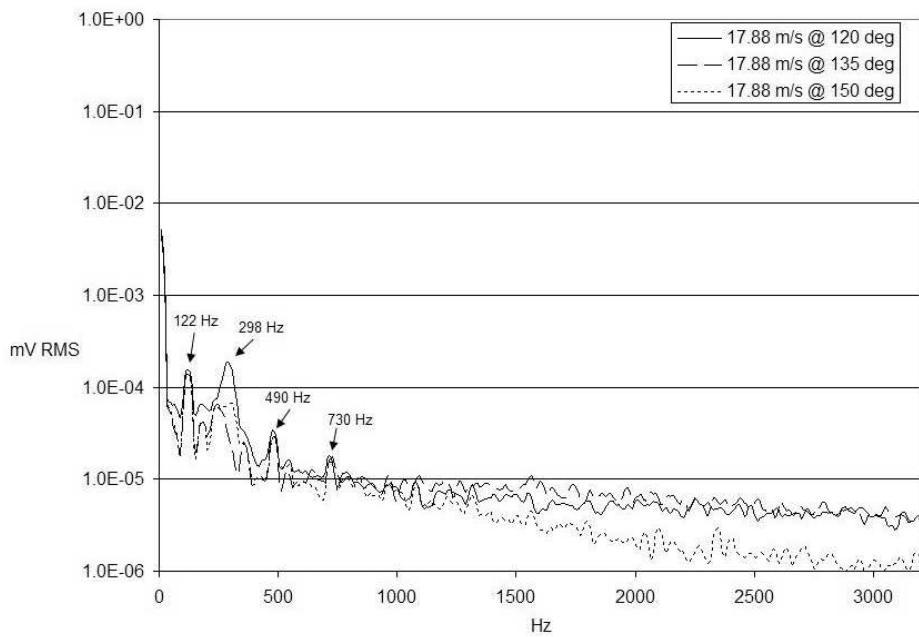

Figure 4.15: Pressure frequency response of 1 five cylinder array from 120° to 150° in 17.88 $\frac{m}{s}$ tunnel indicated flow with a turbulence grid installed.
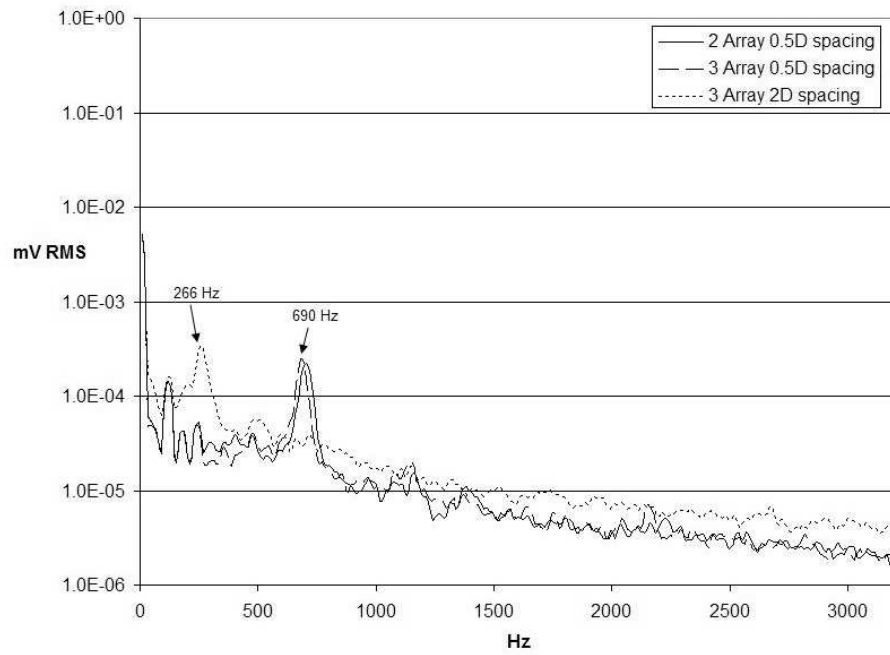
Figure 4.16:   Pressure frequency response of 2 and 3 full arrays at 150° in 20 $\frac{m}{s}$ tunnel indicated flow with no turbulence grid installed.
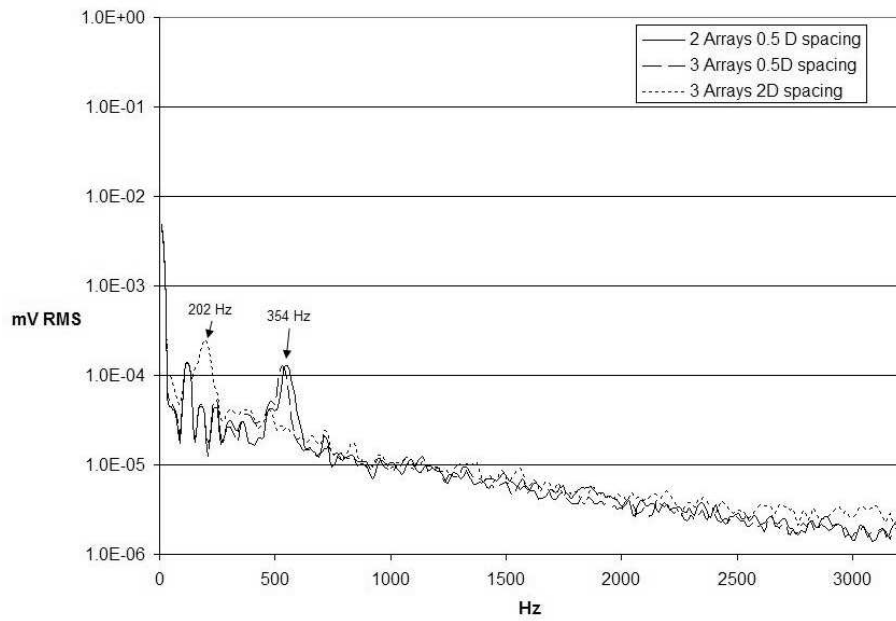

Figure 4.17:   Pressure frequency response of 2 and 3 full array at 150° in 16.54 $\frac{m}{s}$ tunnel indicated flow with a turbulence grid installed.

Table 4.6:   Frequency Response Strouhal Numbers.

	Tunnel Indicated Velocity, $\frac{m}{s}$	Equivalent Hot-wire Velocity, $\frac{m}{s}$	Freq. Hz	St	Re
1 Cyl No Grid	26.0	29.5	242	0.21	53,285
1 Cyl No Grid	49.0	56.0	434	0.19	101048
1 Cyl w/ Grid	22.8	22.4	234	0.26	40,473
1 Array No Grid	29.0	32.2	586	0.46	58,066
1 Array w/ Grid	17.9	17.3	298	0.44	31,289
Multiple Array No Grid	20.0	21.6	266	0.31	38,958
Multiple Array w/ Grid	16.5	16.0	202	0.32	28,781

Strouhal numbers were calculated for the first predominant frequencies seen in each of the cases. Other than the outlier in the one array with no grid configuration, as discussed above, all frequencies were in the same general range, 200-300Hz. For all of these cases, the Reynolds number was in the range of 30,000-50,000, and the Strouhal numbers were in the range of 0.20-0.40, with the one array, no grid outlier up around 0.45. There is a predominant recurrence of strouhal numbers in the range of 0.20-0.30. These numbers are tabulated in Table 4.6. This range is historically typical of Strouhal numbers associated with Reynolds number in the range of 800-200,000.

Matching Strouhal numbers to historical experience presents a level of confidence in collecting reasonable data and obtaining a true characterization of the flow. As Reynolds number was used as a means to reference the configurations with multiple arrays and cylinders, the Strouhal number too is used in such away. Reynolds and Strouhal numbers are non-dimensional parameters used to categorize single cylinders in uniform flow. Achieving Reynolds and Strouhal numbers in the vicinity of the typical values for a single cylinder case validates the similarities across the configurations.

V. Conclusion

The goal of this project was to establish a comparison between flow effects with and without a turbulence grid upstream of generic engine nacelle clutter. This work contributes to the development of fire suppressant technologies by adding to the understanding of turbulent flow around obstructions. Better fire suppression technologies lead to a more efficient application of halon 1301 replacements.

5.1 Experimental Set-up

In order to perform this experiment a number of different instruments had to be configured. Each of the model pieces was designed and sent to the AFIT model shop for fabrication. The Aerolab wind tunnel was configured and supplied with power by the AFIT lab technicians. Once set-up, the Dantec hot-wire system was calibrated and the Aertech traverse system was set up. In addition, the pressure transducer was calibrated and mounted such that the wires and reference pressure port could be accessed from outside the tunnel. Finally, the HP spectrum analyzer was checked and made ready for testing.

During setup, calibration, and configuration, care was taken to ensure consistency between tests from day to day. Equally, attention to detail ensured that a significant level of validation was obtained. However, as with any test, a level of uncertainty was present due to outside sources. These sources include, but are not limited to, simple items such as signal noise and non perfect conditions that exist in a lab facility. Other, more significant, outside influences could include wind tunnel vibrations, system interpretability, and instrumentation placement accuracy. Luckily, the repeated patterns that emerged and results that matched historical trends confirmed that the results obtained were a valid demonstration of flow past generic clutter items.

5.2   Pressure and Velocity Results

The turbulence grid added a 6-7% turbulence intensity to each of the test cases. This was close to the 10% value for the wind tunnel used by Disimile, et al., in work conducted at the 46^{th}TW [11]. Likewise, this matches other previous work such as 6% Takahasi, et al. [20], and 3-5% by Romberg and Popp [19].

Velocity measurements taken with the hot-wire system across a vertical traverse behind 1 cylinder and three arrays at a Re number of approximately 24,000 showed analogous patterns. The wake was characterized behind the model and TI ranged from 25-30%. This showed a great deal of mixing in the recirculation zone behind the obstructions. The mean streamwise velocity was lowest behind the obstruction and highest past the top and bottom edges of the cylinder. In addition, perturbations were highest behind the cylinder for one cylinder as well as the three array configurations.

Mean pressure measurements showed that upstream turbulence caused the front surface of the obstructions to experience lower pressures than non-turbulent upstream flows. This lower pressure continued around the circumference of the cylinder. When additional clutter was present a noticeable effect on the magnitude of the pressure drop was seen at the separation points. This was most likely due to increased velocities of airflow traveling in between cylinders. However, as space was added in between clutter arrays the flow around the cylinders slowed slightly. Pressure data was all validated by matching Strouhal numbers to typical ranges for similar Reynolds numbers.

5.3   Recommendations for Future Work

The intent of this research was to provide insight to the flow characteristics inside an engine nacelle. This characterization can now be used to assist in further prediction of flame properties in adverse nacelle environments. Likewise, this understanding can be applied to the design of more efficient fire suppression delivery systems. Ultimately, this will lower weight and cost of the entire platform.

While this research was a good baseline into a comparison of the effects of upstream turbulence on the flow field around downstream obstructions, further investigation should be conducted. One area of investigation could be the effects of wind tunnel vibrations and signal noise on the accuracy of test results.

Another area to investigate further is the velocity profiles in the tunnel and around the cylinders. For example, doing a traverse of the entire height of the tunnel test section would give a profile of the tunnel. This would show if the asymmetric traverse results were an effect of the tunnel or the model and grid. Likewise, going further past ±20mm from the centerline of the tunnel will provide a better characterization of the cylinder wake. Also, it will show if the flow profiles become more symmetric when data is collected further away from the cylinder. Further investigation could also be put into the shift that was seen in the traverse data. This would show whether the shift occurred as a flow effect or from loses associated with the tunnel.

Pressure data could be gathered at locations other than the front center cylinder for multiple configurations. This would provide insight into whether or not similar effects are seen within obstructions. This investigation would reveal if pressure differentials or vortex shedding occurred at the same rate and magnitude, as well as the same circumferential location, throughout the different cylinders.

Appendix A. Hot-wire Velocity Extrapolation and Conversion Charts

Table A.1:   Airspeed reference and conversion table without a turbulence generation grid. Extrapolated values are presented in bold.

Wind Tunnel Airspeed Indicated mph	Wind Tunnel Airspeed Converted to $\frac{m}{s}$	Hot-wire U_{Mean} Measured $\frac{m}{s}$	Hot-wire U_{Mean} Converted to mph
11.2	5.01	4.37	9.78
22.4	10.01	10.16	22.72
30	13.41	**13.95**	**31.21**
40	17.88	18.95	42.38
45	20.12	**21.59**	**48.30**
60	26.82	29.53	66.06
65	29.06	**32.18**	**71.98**
110	49.17	**56.0**	**125.26**

Table A.2:   Airspeed reference and conversion table with a turbulence generation grid. Extrapolated values are presented in bold.

Wind Tunnel Airspeed Indicated mph	Wind Tunnel Airspeed Converted to $\frac{m}{s}$	Hot-wire U_{Mean} Measured $\frac{m}{s}$	Hot-wire U_{Mean} Converted to mph
11.2	5.01	4.38	9.81
22.4	10.01	9.20	20.58
30	13.41	**12.71**	**28.44**
37	16.54	**15.95**	**35.68**
40	17.88	17.34	38.78
51	22.80	**22.43**	**50.17**
52	23.25	22.89	51.20

Appendix B. Additional Wind Tunnel and Model Photos
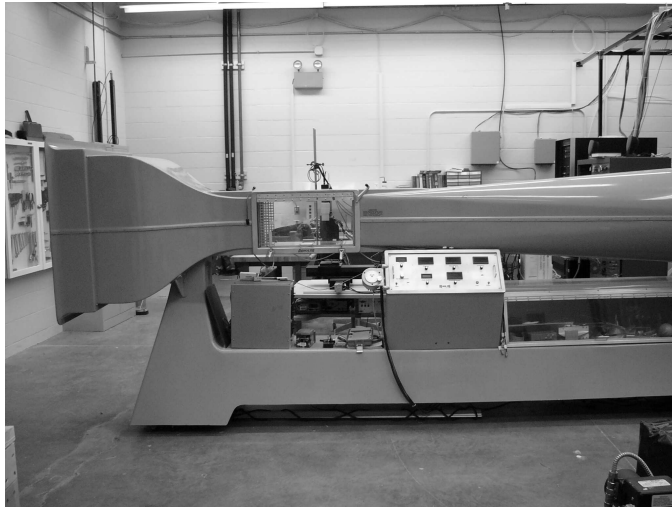

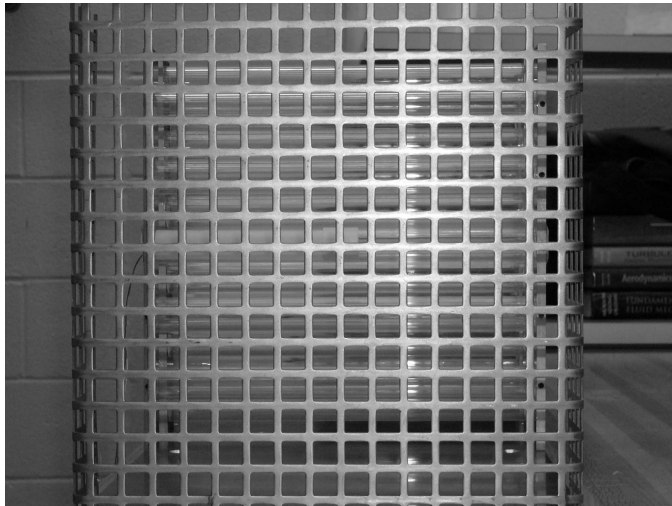Figure B.1:   Side view photograph of the Aerolab wind tunnel.

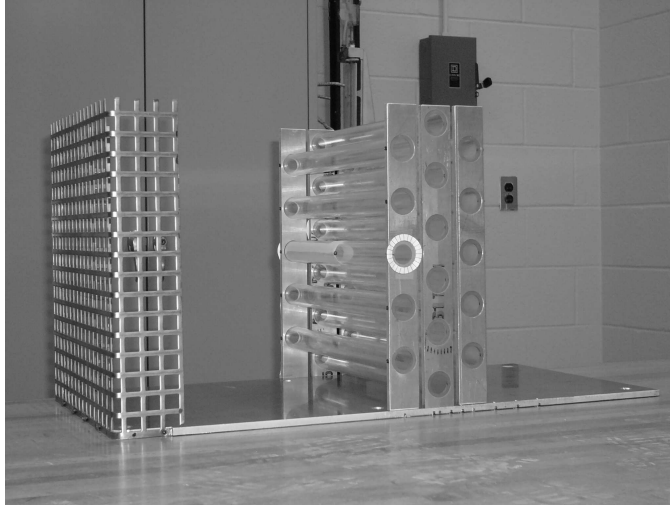Figure B.2:   Front view photograph of the turbulence generation grid.

Figure B.3:   Photograph of the complete model assembly. Shown with a 0.5D spacing and a flow direction of left to right.
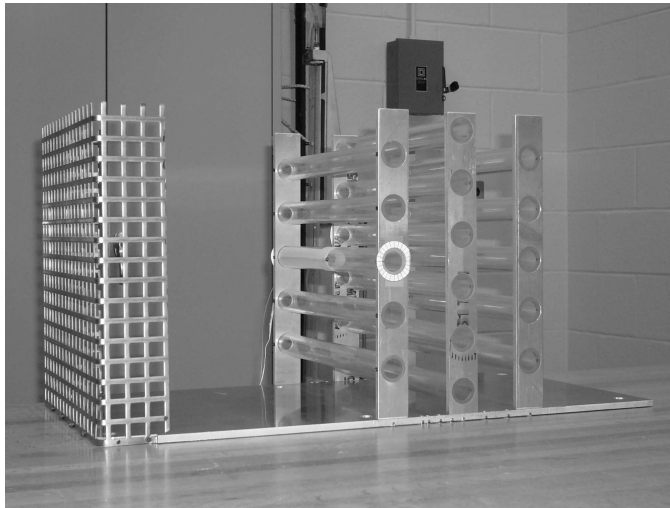

Figure B.4:   Photograph of the complete model assembly. Shown with a 2D spacing and a flow direction of left to right.
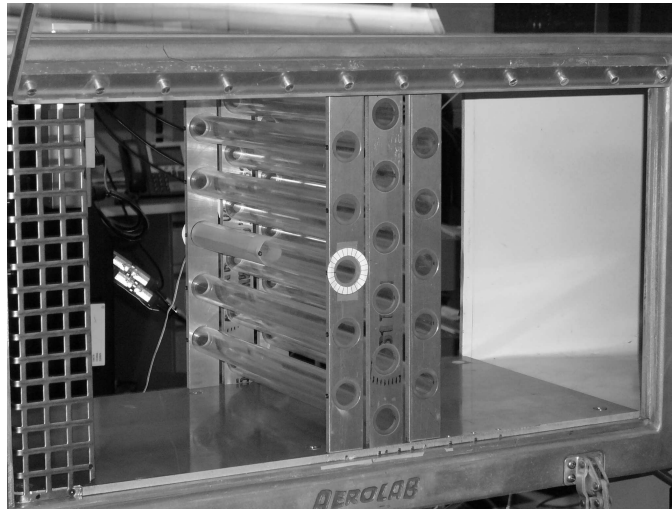
Figure B.5:   Photograph of the entire model assembly installed in the wind tunnel. A 0.5D spacing is shown with downstream angle of view.
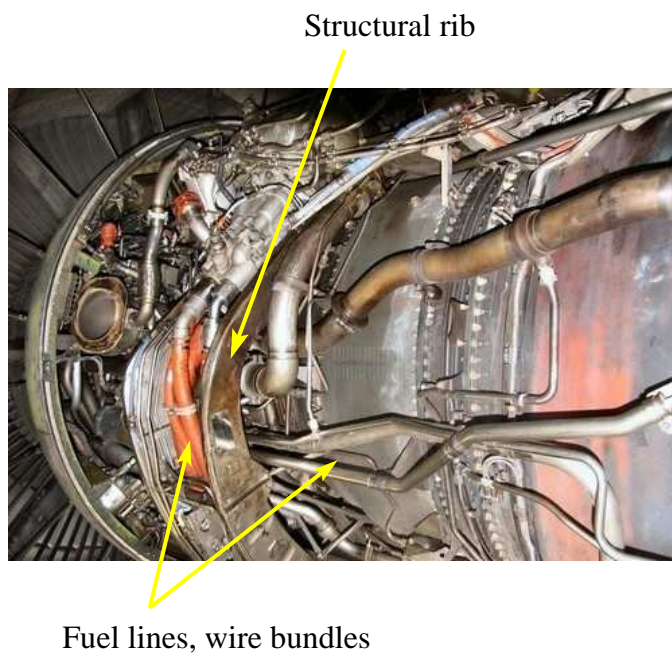
Structural rib

Fuel lines, wire bundles

Figure B.6:   Photograph of typical clutter inside an engine nacelle.

Bibliography

1. "Extinction of Bluff-Body Stabilized Diffusion Flames". *Proceedings of the 1998 Technical Meeting of the Central States Section of the Combustion Institute.* 300 College Park, Dayton, OH, 1998.

2. "Next Generation Fire Suppression Technology Program: FY2005 Progress". Richard G. Gann (editor), *Halon Options Technical Working Conference, 15th Preceedings.* Building and Fire Laboratory, NIST, Gaithersburg, MD, 2005.

3. ACS Industries, LP, Houston, TX. *The Engineered Mist Eliminator*, 2004. Separations & Mass-Transfer Products.

4. Barlow, Jewel B., Jr. William H Rae, and Alan Pope. *Low-Speed Wind Tunnel Testing.* John Wliey & Sons, Inc., New York, NY, third edition, 1999.

5. Bernard, Peter S. and James M Wallace. *Turbulent Flow Analysis, Measurement, and Prediction.* John Wiley & Sons, Inc., Hoboken, NJ, first edition, 2002.

6. Bertin, John J. and Michael L. Smith. *Aerodynamics for Engineers.* Prentice-Hall, Inc., Upper Saddle River, NJ, third edition, 1998.

7. Brantley, Beau M. *Quantitative Analysis of a Turbulent Wind Tunnel with Obstructions for Use in Liquid Flame Spread Experiments.* Master's thesis, Graduate School of Engineering and Management, Air Force Institute of Technology (AETC), Wright-Patterson AFB OH, March 2006. AFIT/GAE/ENY/06-M04.

8. Crawford, B., J.K. Watterson, S. Raghunathan, and J. Warnock. "Modelling the Dispersion of a Fire Suppressant Through an Idealized Nacelle". American Institute of Aeronautics and Astronautics, Belfast, Ireland, January 2006.

9. Dantec Dynamics. *Hot-wire Anemometry.* Guide to explain the use of CTA.

10. Disimilie, Peter J. and John M. Davis. "Characterization of a 2-D Pool Fire Simulator". 46th Test Wing, WPAFB.

11. Disimilie, Peter J., James R. Tucker, Brian Croswell, and John M. Davis. "The Transportation of Water Sprays Past Generic Clutter Elements Found Within Engine Nacelles". *Fire Safety Journal*, 40:65–78, May 2005.

12. Glassman, Irvin. *Combustion.* Academic Press, New York, NY, third edition, 1996.

13. Grosshandler, W., C. Presser, D. Lowe, and W. Rinkinen. "Assessing Halon Alternatives ofr Aircraft Engine Nacelle Fire Suppression". *Journal of Heat Transfer*, 117:489–494, May 1995.

14. Hamins, A., D. Bagdadi, P. Bothwick, M. Glover, W. Grosshandler, D. Lowe, L. Melton, and C. Presser. "Suppression of Simulated Engine Nacelle Fires". *NIST Annual Coonference on Fire Research: Book of Abstracts*, 8–9, 1994.

15. Iwaki, C., K.H. Cheong, H. Monji, and G. Matsui. "PIV Measurements of the Vertical Cross-Flow Structure Over Tube Bundles". *Experiments in Fluids*, 37:350–363, June 2004.

16. Jørgensen, Finn E. *How to Measure Turbulence with Hot-Wire Anemometers*. A Practical Guide 9040U6151, Dantec Dynamics, Skovlunde, Denmark, February 2002.

17. Longstreth, J.D.(USA), F.R. de Gruijl (The Netherlands), M.L. Kriple (USA), Y. Takizawa (Japan), and J.C. van der Leun (The Netherlands). "Effects of Increased Solar Ultraviolet Radiation on Human Health", November 1994. 12 February 2007 http://sedac.ciesin.columbia.edu/ozone/UNEP/UNEP94toc.html.

18. Munson, Bruce D., Donald F. Young, and Theodore H. Okiishi. *Fundamentals of Fluid Mechanics*. John Wiley & Sons, Inc., New York, third edition, 1998.

19. Romberg, O. and K. Popp. "the Influence of Upstream Turbulence on the Stability Boundaries of a Flexible Tube in a Bundle". *Journal of Fluids and Structures*, 12:153–169, December 1998.

20. Takahashi, Fumiaki, W. John Schmoll, Edward A. Strader, and Vincent M. Belovich. "Suppression of a Nonpremixed Flame Stabalized by a Backward-Facing Step". *Combustion and Flame*, 122:105–116, 2000.

21. Vitali, Juan. "Halon Substitute Protects Aircres and the Ozone Layer". *AFRL Horizons*, December 2000.

22. White, Frank M. *Viscous Fluid Flow*. McGraw-Hill, Inc., New York, NY, first edition, 1974.

| 1. REPORT DATE (DD-MM-YYYY)
22 Mar 07 | 2. REPORT TYPE
Master's Thesis | 3. DATES COVERED (From – To)
1 Sept 06 – 22 Mar 07 |
|---|---|---|

| 4. TITLE AND SUBTITLE

Experimental Characterization of Turbulent Flow Around Cylinder Arrays	5a. CONTRACT NUMBER
	5b. GRANT NUMBER
	5c. PROGRAM ELEMENT NUMBER
6. AUTHOR(S)

Harder, Adam, D., Captain, USAF | 5d. PROJECT NUMBER |
| | 5e. TASK NUMBER |
| | 5f. WORK UNIT NUMBER |

| 7. PERFORMING ORGANIZATION NAMES(S) AND ADDRESS(S)
Air Force Institute of Technology
Graduate School of Engineering and Management (AFIT/EN)
2950 Hobson Way
WPAFB OH 45433-7765 | 8. PERFORMING ORGANIZATION REPORT NUMBER

AFIT/GAE/ENY/07-M12 |
|---|---|

| 9. SPONSORING/MONITORING AGENCY NAME(S) AND ADDRESS(ES)
46TW/OG/OGM/OL-AC
Attn: Dr. Peter J. Disimile
2700 D St. Bldg 1661
WPAFB OH 45433-7605 DSN: 785-6302 ext 212	10. SPONSOR/MONITOR'S ACRONYM(S)
	11. SPONSOR/MONITOR'S REPORT NUMBER(S)

12. DISTRIBUTION/AVAILABILITY STATEMENT

APPROVED FOR PUBLIC RELEASE; DISTRIBUTION UNLIMITED.

13. SUPPLEMENTARY NOTES

14. ABSTRACT
This research was done as part of an effort to develop alternative fire suppressant technologies for aircraft engine nacelles. A circular cylinder array was designed, built, and placed in the AFIT roll-around low speed wind tunnel to model generic clutter inside an engine nacelle. A turbulence grid was fabricated to enable measurements of the effects of turbulence level, independent of airspeed, on the flow over different model configurations. The wind tunnel test section was 12 inches wide x 12 inches high x 24 inches long. Pressure differential measurements were taken on various cylinder configurations. The configurations included one cylinder as well as one, two, and three arrays of cylinders. Half diameter spacing was used for two and three cylinder cases, as well as an additional case at a two-diameter spacing with the three array configuration. All conditions were tested with and without the turbulence grid placed at the front of the test section. Pressure differential measurements were taken at 15° increments from 0°-180° on the circumference of on an upstream cylinder, centered vertically on the array. Hot-wire measurements were taken with and without the turbulence grid to determine airspeed and the effect of turbulence intensity generated by the grid on the wake profile. Also, vertical traverse data was taken with the hot-wire to determine airflow characteristics behind two configurations, both with and without a turbulence grid. The first had only one cylinder installed while the second was done with three arrays spaced at a half-diameter length. Pressure and velocity measurements were used to investigate the effects caused by the upstream turbulence grid.

15. SUBJECT TERMS
Turbulence, Flow Characterization, Staggered Cylinder Arrays, Pressure Differential, Velocity Profile, Hot-wire CTA, Vertical Traverse, Turbulence Intensity, Experimental, Engine Nacelle, Fire Suppression.

| 16. SECURITY CLASSIFICATION OF: | | | 17. LIMITATION OF ABSTRACT | 18. NUMBER OF PAGES | 19a. NAME OF RESPONSIBLE PERSON
Dr. Mark F. Reeder |
|---|---|---|---|---|---|
| REPORT
U | ABSTRACT
U | c. THIS PAGE
U | **UU** | 73 | 19b. TELEPHONE NUMBER (Include area code)
(937) 255-3636, ext 4530; e-mail:
mark.reeder@afit.edu |